ANTIBACTERIAL PROPERTIES AND OSTEOBLAST INTERACTIONS OF MICROFLUIDICALLY SYNTHESIZED CHITOSAN – SPION COMPOSITE NANOPARTICLES UNDER EXTERNAL STATIC MAGNETIC FIELD

A THESIS SUBMITTED TO
THE GRADUATE SCHOOL OF NATURAL AND APPLIED SCIENCES
OF
MIDDLE EAST TECHNICAL UNIVERSITY

BY

MELİSA KAFALI

IN PARTIAL FULFILLMENT OF THE REQUIREMENTS
FOR
THE DEGREE OF MASTER OF SCIENCE
IN
METALLURGICAL AND MATERIALS ENGINEERING

AUGUST 2022

Approval of the thesis:

ANTIBACTERIAL PROPERTIES AND OSTEOBLAST INTERACTIONS OF MICROFLUIDICALLY SYNHTESIZED CHITOSAN – SPION COMPOSITE NANOPARTICLES UNDER EXTERNAL STATIC MAGNETIC FIELD

submitted by **MELİSA KAFALI** in partial fulfillment of the requirements for the degree of **Master of Science in Metallurgical and Materials Engineering, Middle East Technical University** by,

Prof. Dr. Halil Kalıpçılar
Dean, Graduate School of **Natural and Applied Sciences** _____

Prof. Dr. Ali Kalkanlı
Head of the Department, **Metallurgical and Materials Eng.** _____

Assoc. Prof. Dr. Batur Ercan
Supervisor, **Metallurgical and Materials Engineering, METU** _____

Assist. Prof. Dr. E. Yegan Erdem
Co-Supervisor, **Mechanical Engineering, Bilkent University** _____

Examining Committee Members:

Prof. Dr. Abdullah Öztürk
Metallurgical and Materials Engineering, METU _____

Assoc. Prof. Dr. Batur Ercan
Metallurgical and Materials Engineering, METU _____

Assoc. Prof. Dr. Erhan Bat
Chemical Engineering, METU _____

Assist. Prof. Dr. Cem Bayram
Department of Nanomaterial and Nanomedicine,
Hacettepe University _____

Assoc. Prof. Dr. Emre Büküşoğlu
Chemical Engineering, METU _____

Date: 18.08.2022

I hereby declare that all information in this document has been obtained and presented in accordance with academic rules and ethical conduct. I also declare that, as required by these rules and conduct, I have fully cited and referenced all material and results that are not original to this work.

Name Last name: Melisa Kafalı

Signature:

ABSTRACT

ANTIBACTERIAL PROPERTIES AND OSTEOBLAST INTERACTIONS OF MICROFLUIDICALLY SYNHTESIZED CHITOSAN – SPION COMPOSITE NANOPARTICLES UNDER EXTERNAL STATIC MAGNETIC FIELD

Kafalı, Melisa
Master of Science, Metallurgical and Materials Engineering
Supervisor: Assoc. Prof. Batur Ercan
Co-Supervisor: Assist. Prof. E. Yegan Erdem

August 2022, 70 pages

In this research, a multistep microfluidic reactor was used to fabricate chitosan-superparamagnetic iron oxide composite nanoparticles (Ch - SPIONs) to develop antibacterial agents that can be targeted to infection foci and visualized with magnetic resonance imaging. Monodispersed Ch – SPIONs had an average particle size of 8.8 ± 1.2 nm with a magnetization value of 32.0 emu/g. These nanoparticles were used to fight against *Staphylococcus aureus* (*S. aureus*) and *Pseudomonas aeruginos*a (*P. aeruginosa),* which are dangerous pathogens that cause tissue and biomedical device-related infection. While Ch – SPIONs showed up to 2 – fold reduction in colonies for both bacteria strains at 0.1 g/L concentration, up to 5 – fold reduction in colonies was observed upon the application of 0.4 T magnetic field for the same concentration of nanoparticles. In addition, osteoblasts were viable and proliferated up to 7 days upon their interaction with Ch – SPIONs in vitro both in the absence and presence of magnetic field. Lastly, Ch – SPIONs reduced T_1 and T_2 signal intensity in magnetic resonance imaging (MRI). Results cumulatively showed

that Ch – SPIONs is a potential candidate as a cytocompatible and antibacterial agent that can be targeted to biofilm bacteria and imaged using MRI.

Keywords: Microfluidics, Antibacterial, Magnetic Field, Osteoblast, Magnetic-Resonance Imaging

ÖZ

MİKROAKIŞKAN YÖNTEMİ İLE SENTEZLENMİŞ KİTOSAN SUPERPARAMANYETİK DEMİR OKSİT KOMPOZİT NANOPARÇACIKLARININ DIŞ STATİK MANYETİK ALAN ALTINDA ANTİBAKTERİYEL ÖZELLİKLERİ VE KEMİK HÜCRESİ ETKİLEŞİMLERİ

Kafalı, Melisa
Yüksek Lisans, Metalurji ve Malzeme Mühendisliği
Tez Yöneticisi: Doç. Dr. Batur Ercan
Ortak Tez Yöneticisi: Dr. E. Yegan Erdem

Ağustos 2022, 70 sayfa

Bu araştırmada, enfeksiyon odaklarına hedeflenebilen ve manyetik rezonans görüntüleme (MRI) ile görselleştirilebilen antibakteriyel ajanlar geliştirmek amacıyla kitosan – süperparamanyetik demir oksit kompozit nanoparçacıklarını (Ch – SPIONs) üretmek için çok aşamalı bir mikroakışkan reaktör kullanıldı. Her biri yaklaşık olarak eşit büyüklükte olan Ch – SPIONs, 8.8 ± 1.2 nm ortalama parçacık boyutuna ve 32.0 emu/g manyetizasyon değerine sahiptir. Bu nanoparçacıklar, doku ve biyomedikal cihaza bağlı olarak gerçekleşen enfeksiyonlara sebebiyet veren *Staphylococcus aureus* (*S. aureus*) ve *Pseudomonas aeruginosa* (*P. aeruginosa*) ile savaşmak için kullanılmıştır. Ch – SPIONs nanoparçacıkları, 0.1 g/L konsantrasyonda, her iki bakteri suşu için kolonilerde 2 kata kadar azalmaya sebep olurken, aynı nanoparçacık konsantrasyonunda 0.4 T manyetik alan uygulanmasıyla kolonilerde 5 kata kadar azalma gözlemlenmiştir. Ek olarak, Ch – SPIONs etkileşimi sonrası kemik hücreleri canlığını korumuş ve 7 güne kadar çoğalmışlardır. Son olarak, Ch – SPIONs, MR görüntüleme cihazında T_1 ve T_2 sinyal yoğunluğunu

azalttı. Elde edilen sonuçlar analiz edildiğinde, Ch – SPIONs nanoparçacıkları, bakterilerin oluşturduğu biyofilm tabakasını hedefleyebilen ve MRI kullanılarak görüntülenebilen, kemik hücreleri ile uyumlu ve antibakteriyel etki gösteren potansiyel bir ajan olduğu gösterilmektedir.

Anahtar Kelimeler: Mikroakışkan, Antibakteriyel, Manyetik Alan, Kemik Hücresi, Manyetik Rezonans Görüntüleme

To my beloved my parents…

ACKNOWLEDGMENTS

I wish to express my deepest gratitude to my supervisor Assoc. Prof. Batur Ercan who gave me the golden opportunity to do many research studies except for my thesis and provided guidance throughout these studies including my thesis subject with his immense academic vision. Thanks to his guidance, advice, criticism, encouragements, and insight throughout the research. His dynamism, vision, sincerity, and motivation have inspired me. It was a great privilege and honor to study under his guidance. I am grateful for what he has offered me.

I would also like to thank Assist. Prof. E. Yegan Erdem for her suggestions, comments, and academic vision. Thanks to her creative research ideas, sincerity, enthusiasm, immense knowledge, and support, I learnt many things from her about microfluidics since starting from my master's degree.

I thank each member of Biomaterial and Nanomedicine laboratory to create peaceful research environment. Also, I am thankful to my friends in Middle East Technical University: Cansu Taşar, Yağmur Göçtü and Alper Haliloğlu for their friendship, for sleepless night, we were working together before deadlines, and we had fun times together in last three years. I am grateful to Gizem Karaaslan for being hardworking undergraduate researcher.

I would like to thank the members of Central Laboratory of Middle East Technical University and Department of Metallurgical and Material Engineering, especially Nilüfer Özel for her help in XRD and Serkan Yılmaz for his help in SEM.

I have special thanks to my friends Melis Keskin and Büşra İşsever since childhood years. You always encourage me and make me happy in my social life. Although you have high workloads, you are always next to me and supportive for everything. I am sure that I need all of you forever in my life. Most significantly, I would like to

express my gratitude and thanks to Murat Yüksel for his endless love, support, encouragement, and understandings.

Finally, I would like to thank my family: my parents Semra Kafalı and Ali Kafalı for their dedication, patience, caring, sacrifices, love and support me spiritually throughout my whole life. In addition, I have special thanks to my grandmother, Ayşe Buluş for growing up me at the first place and her caring, support, and love.

TABLE OF CONTENTS

ABSTRACT v

ÖZ vii

ACKNOWLEDGMENTS x

TABLE OF CONTENTS xii

LIST OF TABLES xv

LIST OF FIGURES xvi

LIST OF ABBREVIATIONS xix

LIST OF SYMBOLS xxi

1 INTRODUCTION 1

1.1 Research Objectives……5

2 LITERATURE REVIEW 7

2.1 Biomedical Device Related Infection……..7

2.2 Contrast Agents for Magnetic Resonance Imaging……10

2.3 Synthesis of Superparamagnetic Iron Oxide Nanoparticles……...12

3 EXPERIMENTAL METHODS 15

3.1 Materials……15

3.2 Device Fabrication……15

3.3 Particle Synthesis……...17

3.4 Characterization of SPIONs and Ch - SPIONs……..20

3.4.1 Scanning Electron Microscopy (SEM)……20

3.4.2 Transmission Electron Microscopy (TEM)……20

3.4.3 X-ray Diffraction……20

3.4.4 Fourier Transform Infrared Spectroscopy……..21

3.4.5 Vibrating Sample Magnetometer……21

3.4.6 Thermogravimetric Analysis……...21

3.4.7 Osteoblast Cell Interaction with SPIONs and Ch - SPIONs...21

3.4.8 Antibacterial Properties of SPIONs and Ch - SPIONs……22

3.4.9 Magnetic Field Simulation……..23

3.4.10 MRI Contrast Agent Performance……24

3.4.11 Statistical Analysis……26

4 RESULTS AND DISCUSSION 27

4.1 Synthesis of SPION and Ch - SPIONs……...28

4.2 Osteoblast Interaction of SPIONs and Ch - SPIONs…….....33

4.3 Antibacterial Properties of SPIONs and Ch - SPIONs……..38

4.4 MRI Contrast Performance of Synthesized Nanoparticles……45

5 CONCLUSION AND FUTURE WORK 47

REFERENCES 51

APPENDICES…….66

A. Fabrication of PDMS Device and SU - 8 Mold……..66

A.1 Silicon Wafer Cleaning…….66

A.2 Preparing of Base Layer……66

A.3 Main Layer Preparation for Microchannel Mold……..68

B. Preparing PDMS Microreactor Using SU - 8 Mold……70

LIST OF TABLES

TABLES

Table 1.1 Advantages and disadvantages of conventional synthesis techniques of SPIONs……...3

Table 2.1 Microorganisms which caused ICU infection..... 7

Table 2.2 The magnitude of the problems of the device related infection…….8

Table 2.3 Pathogens that cause skeletal infectious ……...9

Table 2.4 Industrial T_2 – agent SPIONs……...11

Table 4.1 The size and zeta potentail of both SPIONs and Ch – SPIONs ……..30

Table A.1 Spin Parameters for Base Layer……..66

Table A.2 Pre-baked Parameters for Base Layer……..67

Table A.3 Post Baked Parameters for Base Layer…….67

Table A.4 Spin Parameters for Second Layer……...68

Table A.5 Pre – baked for second layer……68

Table A.6 Post – baked parameters for main layer……69

LIST OF FIGURES

FIGURES

Figure 2.1 T_2 – weighted images were obtained before and after 24 h ferumoxytol administration through lesion area 12

Figure 2.2 SEM images of non-spherical particles which were synthesized with transparent mask. The scale bars are 10 μm……14

Figure 3.1 Fabrication steps of photolitography and bonding of PDMS glass slide ……..16

Figure 3.2 Experimental Set-up: Syringe pumps were used to transfer solutions through capillary tubing……...17

Figure 3.3 Microfluidic PDMS device and microreactor channels…….18

Figure 3.4 **a)** Droplet of iron chloride solution and chitosan solution in the pillar structure before merging, **b)** and **c)** Merging of iron chloride droplet and chitosan droplet, **d)** After merging of these droplets in the pillar structure, iron-chitosan complex formed……...19

Figure 3.5 3-D printed magnetic plate which was used for cell viability test under magnetic field and cell culture plate……23

Figure 3.6 Schematic representation of **a)** magnetic cell culture plate that used for cell viability assay and antibacterial test, **b)** osteoblast cells with SPIONs (black particles) and with Ch – SPIONs (orange particles) under magnetic field, **c)** Magnetic field strength of neodymium magnets, which were used to produce magnetic field for cell culture and antibacterial assay in x, y, and z directions…….23

Figure 3.7 Seven different iron concentration of Ch – SPIONs which were used in MR
imaging…….25

Figure 4.1 Microfluidic synthesis procedure of both SPIONs and Ch – SPIONs ……..27

Figure 4.2 Aggregation behavior of SPIONs and Ch – SPIONs at different points, t=0, 10, 20, 30, 60, 90, 120 minutes……30

Figure 4.3 SEM and TEM images of **a**,**c)** SPIONs, **b**,**d)** Ch – SPIONs . Diffraction pattern of **e)** SPIONs and **f)** Ch – SPIONs. EDX of **g)** SPIONs and h) Ch – SPIONs.……31

Figure 4.4 **a)** XRD graph **b)** FTIR spectra **c)** TGA gravimetric diagram **d)** VSM graph of SPIONs and Ch – SPIONs ……..33

Figure 4.5 Osteoblast (hFOB) cells proliferation without magnetic field for **a)** SPIONs and **c)** Ch – SPIONs , with magnetic field for **b)** SPIONs and **d)** Ch – SPIONs up to 7 days. Values are mean ± SD (n=3), *p< 0.05, **p< 0.01, ***p< 0.005…….36

Figure 4.6 Comparison of hFOB proliferation in the absence and in the presence of magnetic field at 10, 5, 1, 0.5, 0.1 g/L of concentration for **a)** day 1, **b)** day 3, **c)** day 5, and **d)** day 7. Values are mean ± SD (n=3), *p< 0.05, **p< 0.01……37

Figure 4.7 SEM images of hFOB cells on nanoparticles **a)** SPIONs, **b)** Ch – SPIONs without magnetic field, **c)** SPIONs and **d)** Ch – SPION under magnetic field. Scale bars are 20 μm……..37

Figure 4.8 Schematic representation of seven different concentrations of TSB with **a)** SPIONs (black) and **b)** Ch – SPIONs (orange) without magnetic field. Number of colonies for SPIONs against **c)** *S. aureus*, **d)** *P. aeruginosa* and Ch – SPIONs against **e)** *S. aureus*, **f)** *P. aeruginosa* at seven different concentrations for 12, 24 and 48h were shown. Values are mean ± SD (n=3), *p< 0.05, **p< 0.01, ***p< 0.005…….42

Figure 4.9 Schematic representation of seven different concentrations of TSB with **a)** SPIONs (black) and **b)** Ch – SPIONs (orange) with magnetic field. Number of colonies for SPIONs against **c)** *S. aureus*, **d)** *P. aeruginosa* and Ch – SPIONs against **e)** *S. aureus*, **f)** *P. aeruginosa* at seven different concentrations for 12, 24 and 48 h were shown. Values are mean ± SD (n=3), *p< 0.05, **p< 0.01, ***p< 0.005……43

Figure 4.10 *S. aureus* colonies with **a)** SPIONs, **b)** Ch – SPIONs at and *P. aeruginosa* colonies with **c)** SPIONs, **d)** Ch – SPIONs and *S. aureus* colonies with **e)** SPIONs, **f)** Ch – SPIONs at and *P. aeruginosa* colonies with **g)** SPIONs, **h)** Ch – SPIONs at

0.01 g/L concentration growing on agar plate with magnetic field……..44

Figure 4.11 Biofilm assay performed for all concentrations of SPIONs and Ch – SPIONss up to 24 h without magnetic field against **a)** *S. aureus* and **b)** *P. aeruginosa* and with magnetic field against **c)** *S. aureus* and **d)** *P. aeruginosa*. Values are mean ± SD (n=3), **p*< 0.05……45

Figure 4.12 **a)** Example T_1-weighted and T_2-weighted MRI images at 3T. Measured relaxivities were **b)** $r_1 = 0.428\ mM^{-1}\ s^{-1}$ and **c)** $r_2 = 7.764\ mM^{-1}\ s^{-1}$ for Ch – SPIONs at 3T. Graphics display the change in the inverse of T_1 and T_2 relaxation times as a function of iron concentration, for C= [0.68, 1.37, 2.05, 2.74, 4.10, 5.47, 6.84] mM. The error bars designated mean and standard deviation relaxation rates over all pixels in ROIs, dashed line showed linear fit to all data points……46

LIST OF ABBREVIATIONS

ABBREVIATIONS

SPIONs: Superparamagnetic iron oxide nanoparticles

Ch – SPIONs: Chitosan iron oxide composite nanoparticles

MRI: Magnetic resonance imaging

S. aureus: *Staphylococcus aureus*

P. aeruginosa: *Pseudomonas aeruginosa*

ICU: Intensive care unit

PLGA: Poly (lactide – co – glycolide) acid

PDMS: Polydimethylsiloxane

SEM: Scanning electron microscopy

TEM: Transmission electron microscopy

DMEM: Dulbecco's Modified Eagle Medium

FBS: Fetal bovine serum

MTT: 3- (4,5-dimethyl-2-thiazolyl)-2,5-diphenyl-2H-tetrazolium bromide

DMSO: Dimethyl sulfoxide

SAED: Selected area diffraction

XRD: X-ray diffraction

FTIR: Fourier transform infrared spectroscopy

VSM: Vibrational sample magnetometer

TGA: Thermal gravimetric analysis

hFOB: Osteoblast cell line

PBS: Phosphate buffer saline

TSB: Tryptic soy broth

TSA: Tryptic soy agar

TI: Inversion times

TE: Echo times

TR: Repetition times

FOV: Field of view

CV: Crystal violet

ROI: Region of interest

EDAX: Energy dispersive X-ray spectroscopy

ANOVA: Analysis of variance

ROS: Reactive oxygen species

rpm: Revolution per minute

LIST OF SYMBOLS

SYMBOLS

ρ: Proton density

T_1: Longitudinal relaxation

T_2: Transverse relaxation

r_1: relaxivity measured at 12 different inversition time (TI= 24 – 1900 ms)

r_2: relaxivity which were measured at 12 different echo time (TE= 10 – 800 ms).

Fe^{2+}: Iron ion which possess (+2) ionic charge

Fe^{3+}: Iron ion which possess (+3) ionic charge

$FeCl_3.6H_2O$: Ferric chloride hexahydrate

$FeCl_2.4H_2O$: Ferrous chloride tetrahydrate

nm: nanometer

μm: micrometer

d: particle size

λ: wavelength

T: Tesla

C: Concentration of iron ions

θ: Theta

Å: Angstrom

S: Signal intensity

S_0: Scaling factor*spin density

CHAPTER 1

INTRODUCTION

Magnetic nanoparticles have drawn tremendous attention since 1950s in hyperthermia, imaging, drug delivery, and enzyme immobilization applications due to their unique surface chemistry, and magnetic properties [1]. Although there are various types of magnetic nanoparticles, iron oxide nanoparticles have been widely used for specific applications because of their high surface area, superparamagnetism, biocompatibility, magnetic moment, and size uniformity. Superparamagnetic iron oxide nanoparticles (SPIONs) have several features that make them promising for biomedical applications. The first feature is related to their size, which is smaller than 200 nm to provide easy penetration into cells [2]. The second feature is related with the surface properties of SPIONs, which allow easy functionalization with polymers and other materials. The third feature is superparamagnetism. SPIONs do not have any remnant magnetization when external magnetic field is removed [1]. The last feature is that their synthesis method, which should be reproducible, scalable and low cost [3]. Having these properties, SPIONs are used by scientists for various tissue engineering applications.

SPIONs have been synthesized using conventional methods including chemical vapor condensation, co-precipitation, thermal decomposition, microemulsion, and etc [4]. Although there are many different techniques to synthesize SPIONs, these methods have some limitations which are:

- complex synthesis methods,
- expensive and large equipment space requirments,
- fluctuation in synthesis conditions,

- insufficient control over synthesis process and
- long processing times [5].

Due to the limitations of conventional techniques, as stated in Table 1.1, an easy to manipulate technique is required for the efficient synthesis of high quality iron oxide nanoparticles. Owing to various advances in microfluidic synthesis of nanoparticles, most of the limitations in the conventional techniques has been overcome. With efficient control over particle size, microfluidic synthesis provides many benefits, including:

- small capillary dimensions which results in higher surface area to volume ratio [6],
- miniaturization of devices,
- decreased analysis time,
- reduced consumption of reagents,
- increased portability [7],
- formation of uniform and monodispersed particles with a high encapsulation efficiency [8].

The parameters for reaction kinetic for each stage in the nanoparticle synthesis are important to obtain monodispersed nanoparticles.

Table 1.1 Advantages and disadvantages of conventional synthesis techniques for SPIONs [4]

Type of Synthesis	Pros	Cons
Microwave	Short reaction time, higher yields, excellent reproducibility, easy handling	Expensive, unsuitable for scale-up and reaction monitoring
Spray pyrolysis	Finely dispersed particles of predictable size, shape and variable composition	Aggregated particles, expensive
Laser pyrolysis	Small particle size, narrow particle size distribution, near absence of aggregation	Complicated, very expensive
Pulsed wire discharge method	Fast process, higher purity of NPs	Batch process, limited production, high vacuum systems, costly process, contaminations in product
Chemical vapor condensation	Suitable for preparing small quantities to demonstrate desired properties in the laboratory	Low production, difficult to control size and particle size distribution
Co-precipitation	Convenient method, simple and rapid preparative method, easy control of particle size and composition	Extensive agglomeration, poor morphology and particle size distribution
Thermal decomposition	Producing highly monodispersed particles with a narrow size distribution	High cost, long-time synthesis reaction, high temperature
Microemulsion	Monodispersed nanoparticles with various morphology can be produced	Not very efficient and difficult to scale up
Polyol	Uniform size particles can be prepared, easy to scaleup	Needs high temperature, long time
Sol–Gel	Low processing cost, energy efficiency, high production rate, and rapid productivity	Limited efficiency, high cost
Sonochemical	Simple, low cost, safe, environment friendly, absence of many reactants	Very small concentration of prepared NPs, particle agglomeration is very narrow
Biological synthesis of nanoparticles using plants and bacteria	Selectivity and precision for nanoparticle formation, cost effective, eco friendly	Limited knowledge, difficulty in controlling size and properties

The stability and cytotoxicity of microfluidically synthesized SPIONs are important for drug delivery and imaging applications. Some studies show that SPIONs decreased the cell viability in a concentration-dependent manner *in vitro* [9]. For instance, Khalid *et al.* showed that SPIONs damaged the primary hippocampal neural cells at 500 µg/mL concentration [10]. Another study demonstrated that SPIONs had a cytotoxic effect on PC-12 cells when concentration of nanoparticles was greater than 100 µg/mL [11]. In addition to the toxicity of SPIONs, their stability is a crucial factor for their medical use. Although many different types of SPIONs

have been used for medical diagnosis and theraphy, SPIONs have several disadvantages regarding medical usage. For instance, SPIONs can agglomarate which may lead to, in the worst case, reduction or blockage the blood flow in our veins [10], [12]. To overcome these disadvantages, the stability of SPIONs should be improved with several types of coating materials.

One approach to increase stability and decrease toxicity of SPIONs is to encapsulate them with natural or synthetic polymeric materials. In literature, there are various coating materials, including amorphous silica, polyethylene glycol, polyvinyl alcohol, gelatin, starch, dextran, liposomes, etc. [13]. Since coating materials should be biodegradable and biocompatible, chitosan is a promising choice to coat SPIONs. Furthermore, the chitosan backbone has many reactive functional groups, which allow the binding of various agents, and it can act as an anchor for conjugation of imaging agents. During synthesis, the chitosan coating layer was found to limit the growth of iron oxide core, stabilized these nanoparticles in aqueous medium through steric repulsion, and minimized the immune response against SPIONs in the body [14]. Another approach to decrase cytotoxicity of SPIONs is altering their physical properties. When their size and morphology are changed, their interaction with biological tissues differed. For example, nanoparticles having smaller size than 10 nm can be easily removed by renal clearance, while particles larger than 200 nm can be concentrated in the spleen [15]. Furthermore, nanoparticles smaller than 2 nm are not appropriate for medical use because these nanoparticles might damage the cell membrane and intracellular organells [15]. The physical properties of SPIONs not only affect their cytotoxicity but also influence their antibacterial activity against pathogens.

SPIONs can show antibacterial property against both gram positive and gram negative bacteria strains. Because of possessing very small size, they have high surface to volume ratio and high free energy content. To reduce their free energy, they might be interacted with cellular membranes to become stable entities. These

nanoparticles can interact with bacterial cells through hydrophobic and electrostatic interactions and they can pass through the bacterial cell walls [16]. Once they pass through the cell walls, they might generate reactive oxygen species even at low nanoparticle concentrations.

In this study, Ch – SPIONs were synthesized inside microfluidic channels to use them against biomedical device related infection. To understand the activity of these nanoparticles against infection, antibacterial activity and cytocompatibility of microfluidically synthesized Ch – SPIONs were investigated in the absence and in the presence of a magnetic field and potential of these nanoparticles as a MRI contrast agent was explored. The antibacterial activity of nanoparticles was tested against *Staphylococcus aureus* (*S. aureus*) and *Pseudomonas aeruginosa* (*P. aeruginosa*), both of which were the leading cause of tissue and device-related infections. Ch – SPIONs were also interacted with bone cells (osteoblasts) to understand their cytotoxicity. The results identified these nanoparticles to be a potential candidate for the targeting and elimination of biofilm, and the magnetic resonance results of Ch – SPIONs were promising and they can potentially be used as a contrast agent.

1.1 Research Objectives

Although there are a few publications in literature on the microfluidic synthesis of Ch – SPIONs, there is no information on the biological properties of these nanoparticles for biomedical applications. Thus, the objective of this thesis is:

- To synthesize monodisperse Ch – SPIONs nanoparticles via multistep microfluidic technique,
- To characterize physical and chemical properties of the synthesized nanoparticles,
- To assess if Ch – SPIONs can be visualized in MRI,

- To investigate their antibacterial activity with *Staphylococcus aureus* and *Pseudomonas aeruginosa* strains, and cytocompatibility with osteoblast cell line.

CHAPTER 2

LITERATURE REVIEW

2.1 Biomedical Device-Related Infection

Infection is major a problem that causes prolonged treatment durations, increased hospitalization costs, and risk lives of patients [17]. Researchers showed that overall rate of intensive care unit (ICU) infection was 27.6 % - 29 % per 1000 ICU days during a 10-year study in Poland [18]. Based on the published data, half of hospitalized patients were infected in ICUs. The most common microorganisms isolated at ICU are listed in Table 2.1.

Table 2.1 Microorganisms which caused ICU infection [17], [18]

Type of Microorganisms	Percentage of rate of infection (%)
Acinetobacter baumannii	25
Staphylococci	15
Escherichia coli	9
Pseudomonas aeruginosa	8
Klebsiella pneumaniae	7
Candida albicans	6

Aside from ICU, medical devices can also get infected. In the United States, the use of medical devices was associated with cause various diseases, such as pneumonia, bloodstream, and urinary tract infections [18], [19]. Another example for medical device infections is joint protheses. Although the infection rate of them is lower than that of other medical devices, i.e., catheters, their infection management is much

more difficult and expensive. Infections of devices used to treat heart diseases show the highest rate of mortality. All medical devices that are placed in the United States and their rate of infection is shown in Table 2.2.

Table 2.2 The magnitude of the problems for the device related infections [19]

Device	Estimated no. inserted in the United States per year	Rate of infection, %	Attributable mortality[a]
Bladder catheters[b]	>30,000,000	10–30	Low
Central venous catheters[b,c]	5,000,000	3–8	Moderate
Fracture fixation devices[b]	2,000,000	5–10	Low
Dental implants[d]	1,000,000	5–10	Low
Joint prostheses[b]	600,000	1–3	Low
Vascular grafts[b]	450,000	1–5	Moderate
Cardiac pacemakers[b,d]	300,000	1–7	Moderate
Mammary implants, in pairs[e]	130,000	1–2	Low
Mechanical heart valves[d]	85,000	1–3	High
Penile implants[b,d]	15,000	1–3	Low
Heart assist devices[d]	700	25–50	High

[a] Semiquantitative scale for attributable mortality: low, <5%; moderate, 5%–25%; high, >25%.
[b] Numbers estimated by analysis of market reports.
[c] Numbers estimated by review of the medical literature.
[d] Numbers estimated by personal communication with personnel from device manufacturing companies.
[e] Numbers estimated by review of data provided by medical associations.

Although the data listed in Table 2.2 belong to first insertion of the medical devices, the real number of patients is estimated to be higher than it is stated. These reasons are as follows:

1) Reimplantation increases the rate of infection from 1 % to 3 % [21],
2) Explanting part of the infected implant rather than all of it increases the infection rate [22],
3) The use of low-quality implants during medical operations [21],

4) The formation of biofilm on medical devices enhances the infection rate due to the wrong implantation techniques,
5) The use of antibiotics prior to appropriate diagnostic cultures causes possibly false negative results.

Bacteria that colonize medical devices multiply and form biofilms that can be defined as aggregates of bacterial cells enclosed in a self-produced exopolysaccharide matrix to adhere to a surface [23]. Biofilm is a type of bacterial shield against biological attack [24]. Two of main biofilm forming bacteria are *S. aureus* and *P. aeruginosa*, and both strains induce severe diseases, as shown in Table 2.3.

Table 2.3 Pathogens that cause skeletal infectious [25]

Species	Upper Extremity	Vertebral	Trauma or fracture related
Staphylococcus aureus	10-40	15-60	20-40
Pseudomonas spp.	<5	5-10	5-10
Gram-negative	5-10	10-40	20
Fungal	<5	<5	<5

Use of nanomaterials is growing in the fight against planktonic bacteria and biofilms [26]. For example, carbon-based nanoparticles, including graphene, carbon nanotubes [27], [28], and fullerenes, and metal-based nanoparticles, such as silver (Ag), iron oxide (Fe_3O_4), magnesium oxide (MgO), have shown antibacterial properties [26]. Furthermore, magnetic nanoparticles, specifically, SPIONs have bactericidal activity against both planktonic bacteria and biofilm – mass [29].

2.2 Contrast Agents for Magnetic Resonance Imaging

Magnetic resonance imaging (MRI) is a non-invasive imaging technique which is used to diagnose or stage human diseases [30], [31]. To obtain the clarity in MRI

images, contrast agents have been used since 1985. Contrast agents provide an improvement in image contrast between normal and disease tissue by changing the relaxation for protons of water molecules in tissues. MRI contrast agents are sensitive to three tissue parameters, namely proton density (ρ), longitudinal relaxation (T1), and transverse relaxation (T_2). When image sequences are sensitive ρ, they are called proton density-weighed image. Similarly, when image sequences are sensitive to mainly T_1 or T_2 relaxation, they are called T_1 or T_2 relaxation weighted images [32]. They are categorized based on their effect on image, their magnetic behavior and biodistribution in the body [33]. Contrast agents can be divided into mainly two categories which are superparamagnetic and paramagnetic contrast agents [33].

Superparamagnetic contrast agents constitute of mainly iron oxide nanoparticle core and various kinds of polymer coatings, such as dextran, starch, carboxydextran, chitosan, heparin, albumin, and polystyrene [33]. They can be relaxated T_1 or T_2 relaxation times, if contrast agents have high r_2 / r_1 ratio, they are affected T_2 and they are called T_2 – agents or negative contrast agents. Contrast agents that have reverse condition (high r_1 / r_2) are called T_1 – agents or positive contrast agents. While T_1 – agents increase signal intensity, T_2 – agents decrease signal intensity, providing darkened MR images [34] . Their relaxation behavior depends on the size of synthesized SPIONs, and SPIONs having smaller than 10 nm are negative contrast agents. Examples of T_2 – agent SPIONs are shown in Table 2.4 [35].

Table 2.4 Industrial T_2 – agent SPIONs [35]

T_2-agent	Particle diameter (nm)	Relaxivity (mM s)$^{-1}$[a]	Target
Carboxydextran-coated SPIO SHU-555[b]	62	$R_1 = 12$; $R_2 = 188$ (0.94 T)	Reticuloendothelial system's organs (liver)
Dextran-coated SPIO AMI-25[c]	58	$R_1 = 24$; $R_2 = 107$ (0.47 T)	Reticuloendothelial system (liver)
Dextran-coated USPIO MION-46L[d]	18–24	$R_1 = 16$; $R_2 = 35$ (0.47 T)	Reticuloendothelial system (liver)
Dextran-coated USPIO AMI-227[e]	17–20	$R_1 = 23$; $R_2 = 53$ (0.47 T)	Lymph nodes
MION-encapsulated liposomes	170–300	$R_1 = 10$; $R_2 = 130$ (0.47 T)	Reticuloendothelial system's organs (liver)
PEGylated magnetoliposomes	40	$R_1 = 3$; $R_2 = 240$ (1.5 T)	Bone barrow
(Protein-coated) magnetoferritin	12	$R_1 = 8$; $R_2 = 218$ (1.5 T/25 °C)	Blood pool
NC100150[f]	20	$R_1 = 20$; $R_2 = 35$ (20 MHz)	Reticuloendothelial system (liver)
OMP[g]	300–400		Gastrointestinal (GI)
AMI-121[h]	200		Gastrointestinal (GI)
VSOP-C63[i]	2–10	$R_1 = 30$; $R_2 = 39.1$ (1.5 T/37 °C)	Blood pool

[a] Relaxivities were measured at 37 °C and the static magnetic field B_0 expressed in Tesla is noted in parentheses.
[b] Ferucarbotran Resovist® from Schering, Germany.
[c] Endorem® from Guerbet, France or Feridex® from Advanced Magnetics, USA.
[d] Massachusetts General Hospital, Boston, USA.
[e] Sinerem® from Guerbet, France or Combidex® from Advanced Magnetics, USA.
[f] Clariscan®, Nycomed Amersham Imaging, Oslo, Norway.
[g] Nycomed, Oslo, Norway, WIN39996, Winthrop-Sterling, Clariscan®, Nycomed Amersham Imaging, Oslo, Norway.
[h] Ferumoxsil, Advanced Magnetics, Cambridge, MA, USA, Ferropharm Gmbh, Germany.

Superparamagnetic contrast agents contain mainly superparamagnetic iron oxide nanoparticles (SPIONs), and they are divided into three categories based on their particle size (d).

1) If d is smaller than 50 nm, they are called ultra-small SPIONs
2) If d is bigger than 50 nm, they are called SPIONs
3) If d is larger than 200 nm, they are called large particles [34].

Although the first and second categories can be used for intravenous administration, the last category is used for the gastrointestinal tract [35].

As a contrast agent, when size and coating of SPIONs are altered, they can be designed as a tissue-specific contrast agent. For example, ferumoxide and ferucarbotran are liver-specific contrast agents due to their absorption by Kuppfer cells in the liver. Another example of its tissue-specific property is Ferumoxtran – 10, which can be used in the blood pooling due to having a high circulation time [36]–[38]. Exemplary images are shown in Figure 2.1, where ferumoxytol was

injected as an intravenous contrast agent to central nervous system lymphoma area and it showed local and strong signal loss in that area after 24 h [38], [39].

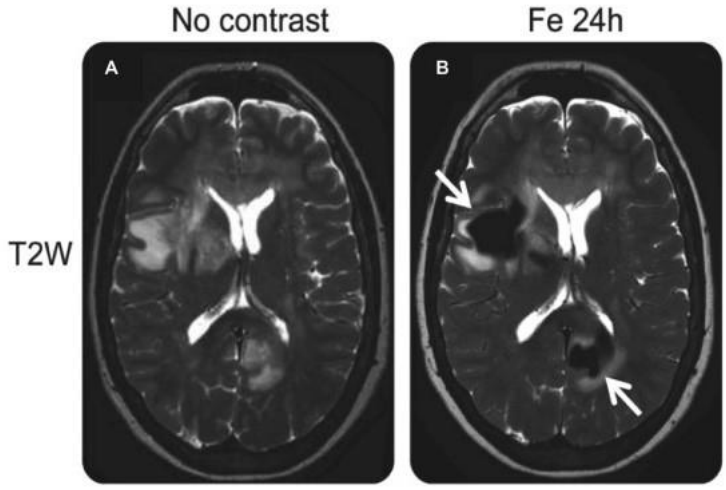


Figure 2.1 T_2 – weighted images were obtained before and after 24 h ferumoxytol administration through lesion area [38], [39].

2.3 Synthesis of Superparamagnetic Iron Oxide Nanoparticles

Among various fabrication techniques, microfluidic synthesis has gained popularity due to providing more control over size, size distribution, and morphology [40]. Briefly, a microfluidic platform utilizes micro or nanoscale production techniques to develop highly controllable fluidic synthesis environment [41]. Microfluidic synthesis comprises of droplet formation, followed by merging them in the channel. Via the surface tension and viscous forces in the channel, droplets of dispersed phase form. Continuous phase, which wets the channel and carries the dispersed phase droplets, surrounds the formed droplets, and eliminates their contact with the channel, which reduces clogging related issues. Mixing time, velocity of fluids and geometries of the microfluidic platform affect the size and size distribution of synthesized nanoparticles in this technique [41].

In the synthesis of Ch – SPIONs in the microreactor, silicon oil was supplied to the channel to obtain hydrophobic channel surfaces prior to initiating the reaction. After

all channel surfaces were wetted with silicon oil, chitosan and iron chloride solutions were supplied and their droplets merged in the channel. While merging these nanoparticles, amine groups of chitosan capture Fe^{2+} and Fe^{3+} ions to form iron – chitosan complex before nucleation step. This complex acts as a barrier to the diffusion of iron ions during the growth phase, providing a smaller iron core and overall particle size [42]. Furthermore, when iron – chitosan complex reacts with ammonia solution, which adjust the pH, reaction takes place and color change was observed. The ammonia solution also improves homogeneity and prevents the formation of agglomeration during crystal growth [43]–[46].

There are many studies in the literature for production of various types of nanoparticles using microfluidic synthesis. For instance, Xu *et al.* produce PLGA droplets in PDMS channels by changing the flow rate of the continuous phase and the dispersed phase. These particles were monodispersed with sizes ranging from 10 μm to 50 μm [47], [48]. Lee *et al.* [48], [49] and Carroll *et al.* [48], [50] synthesized ordered mesoporous silica nanoparticles in a microfluidic device. Geometry of the microfluidic channel, flow rate of the continuous and dispersed phase solutions, and the type of the continuous phase were controlled. Furthermore, Xu *et al.* reported that non – spherical particles, such as rod, ellipse, and disk-shaped particles, could be produced by increasing the volume of the droplets (in Figure 2.2). If volume of droplets exceeded that of the largest sphere, the droplet was deforming into a disk or an ellipsoid or a rod [48], [51].

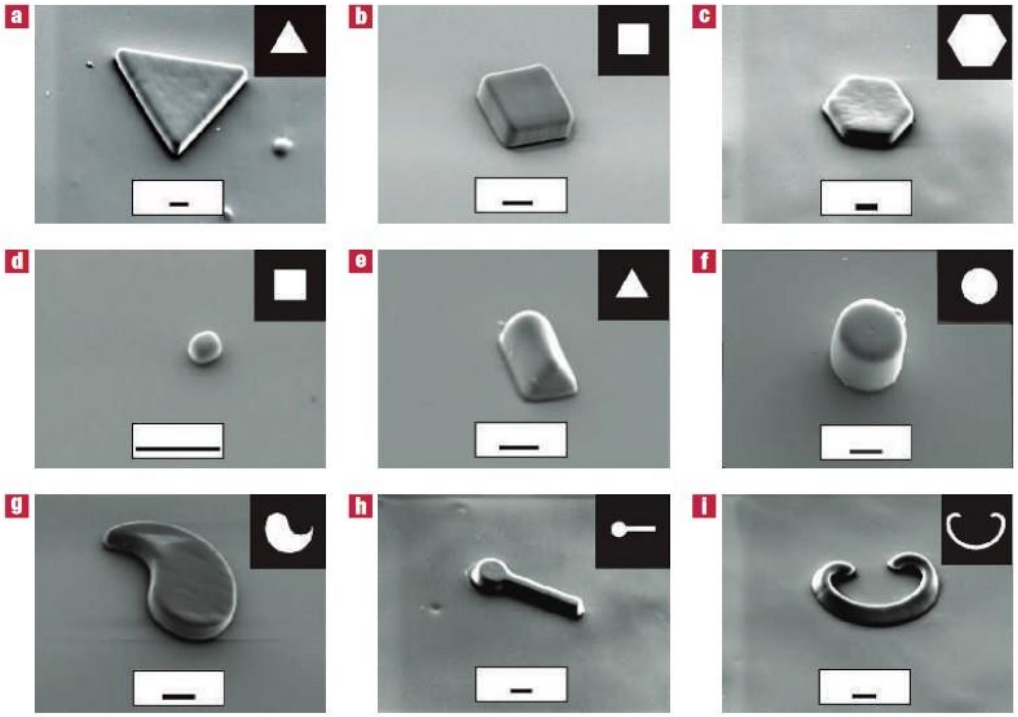


Figure 2.2 SEM images of non-spherical particles which were synthesized with transparent mask. The scale bars are 10 μm [52].

In this thesis, ch – SPIONs composite nanoparticles will be synhtesized. Their properties will be characterized using various analytical techniques. Their antibacterial performance and cytotoxicity will be assessed. In addition, their potential use as MRI contrast agent will be evaluated.

CHAPTER 3

EXPERIMENTAL METHODS

3.1 Materials

All chemicals used in this work were analytical grade. Chitosan, ferric chloride hexahydrate ($FeCl_3.6H_2O$), ferrous chloride tetrahydrate ($FeCl_2.4H_2O$), acetic acid and ammonia (28%) were purchased from Sigma Aldrich. Polydimethylsiloxane was purchased from Sylgard 184 and SU – 8 2005 negative photoresist was purchased from Microresist. Syringe with needle (10 mL) and tubing were purchased from ISOLAB. Single and multichannel syringe pumps (New Era NE-1000) were used for the synthesis. Dulbecco's Modified Eagle Medium (DMEM), penicillin-streptomycin, fetal bovine serum (FBS) and trypsin-EDTA were purchased from Biological Industries (BI). 3- (4,5-dimethyl-2-thiazolyl)-2,5-diphenyl-2H-tetrazolium bromide (MTT) was purchased from Abcam. Dimethyl sulfoxide (DMSO) and hexamethyldisilizane were purchased Sigma Aldrich. Tryptic Soy Broth (TSB) and agar were purchased from Merck.

3.2 Device Fabrication

Device fabrication and experiments were performed at the National Nanotechnology Research Center (UNAM) and microfluidic laboratory located in the Mechanical Engineering Department of Bilkent University.

Microfluidic channels were fabricated in polydimethylsiloxane (PDMS) using the soft lithography technique. PDMS is the most useful elastomer for microfluidic reactors in soft litography. One of the main reasons for using PDMS is the ease of fabrication process, it is also less expensive than silicon or glass, and a more flexible and micrometer scale device can be reproduced with high fidelity in PDMS [7].

Photolithography fabrication steps for the PDMS microreactor are as follows and shown in Figure 3.1, detailed information is stated in Appendix A and B.

1-) The silicon wafer was cleaned using acetone, isopropyl alcohol, and water and dried with nitrogen;

2-) Photoresist was coated by spin coating,

3-) After the prebake step, the photoresist was exposed to UV light,

4-) Channels were formed on the silicon wafer,

5-) The silicon elastomer base and a curing agent in the ratio of 10:1 were mixed and poured into silicon wafer, and they were placed in the vacuum pump for 30 minutes,

6-) They were placed in the oven at 80 °C, then the PDMS layer was peeled off, the inlet and outlet holes were opened and the glass slide to close the channel using plasma treatment [53].

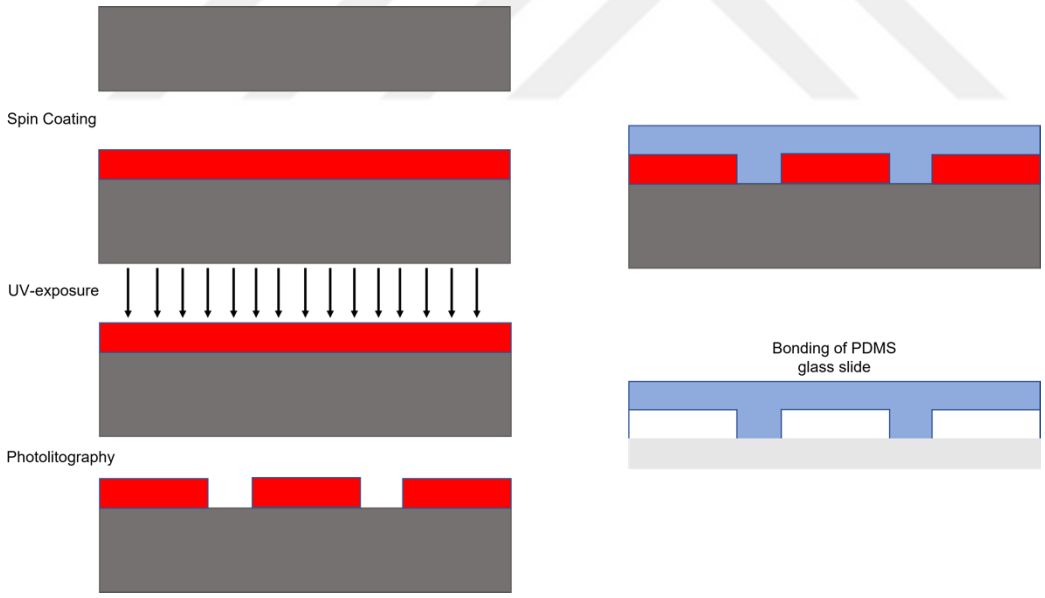


Figure 3.1 Fabrication steps of photolitography and bonding of PDMS glass slide

3.3 Particle Synthesis

The synthesis route of Ch – SPIONs was optimized in previous study where a microreactor was utilized [53]. Before the experiment, iron, ammonia, and chitosan solutions were prepared which were used in the experiment. Firstly, 1.09 g Fe (III) Chloride and 0.4 g Fe (II) Chloride salts were weighted, and they were mixed with 100 mL distilled water. Then, 0.75 g chitosan was dissolved in 100 mL of 0.3 % (v/v) acetic acid, and ammonia solution was diluted by distilled water. For SPIONs synthesis, iron and ammonia solutions were used. Additionally, for Ch – SPIONs, a chitosan solution was used while the iron and ammonia solutions were kept constant. Capillary tubing was used to transport from syringe pump to the inlet of PDMS device. In addition, an inverted microscope was used to monitor the process in the microchannel. The dimensions of microreactor channel were 150 µm x 100 µm, and the width of pillar structure was 335 µm. The angle of double tapered T – junction was 25 °. Experimental set-up was shown in Figure 3.2.

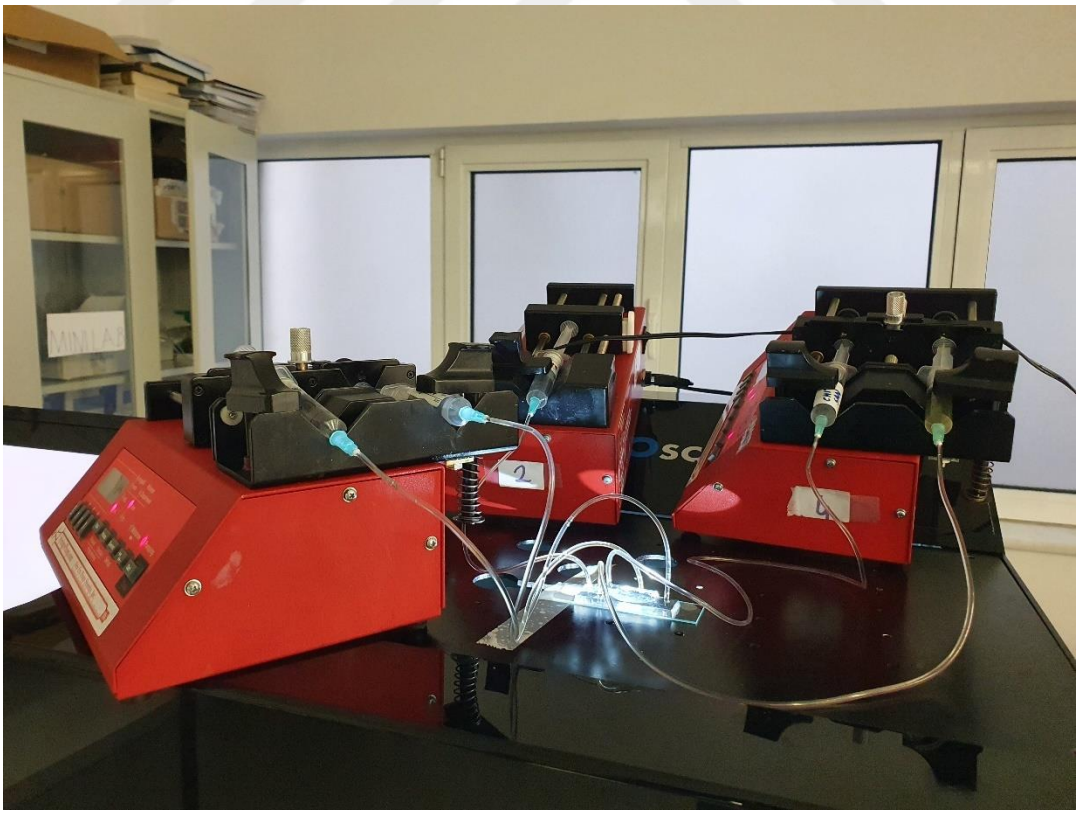


Figure 3.2 Experimental Set-up: Syringe pumps were used to transfer solutions through capillary tubing.

Since the surface of the device became hydrophilic, silicon oil was introduced to inlet of microchannel to obtain a hydrophobic surface. Oil was pumped to microreactor until whole reactor was filled, which facilitates the formation of droplets. After filling the whole device with oil, prepared solutions were supplied to channels and the formation of droplets were observed using an inverted microscopy. During nanoparticle synthesis, the alternating droplet formation of iron and chitosan solutions is crucial to form the iron – chitosan complex in the structure (Figure 3.3). During the production of droplets, the lower stream entered the channel and droplet from that stream formed. Then, the upper stream enters the main channel, and the droplet was generated from the upper stream. After producing these droplets, they were merged in the pillar which slows down the droplets and provides the droplet merging in the channel (Figure 3.4). After the iron and chitosan solutions, ammonia droplets interacted with merged droplets in the channel and SPIONs and Ch – SPIONs were collected at the outlet.

PDMS device and microreactor channels were shown in Figure 3.3 and droplets merging in the pillar structure was shown in Figure 3.4.

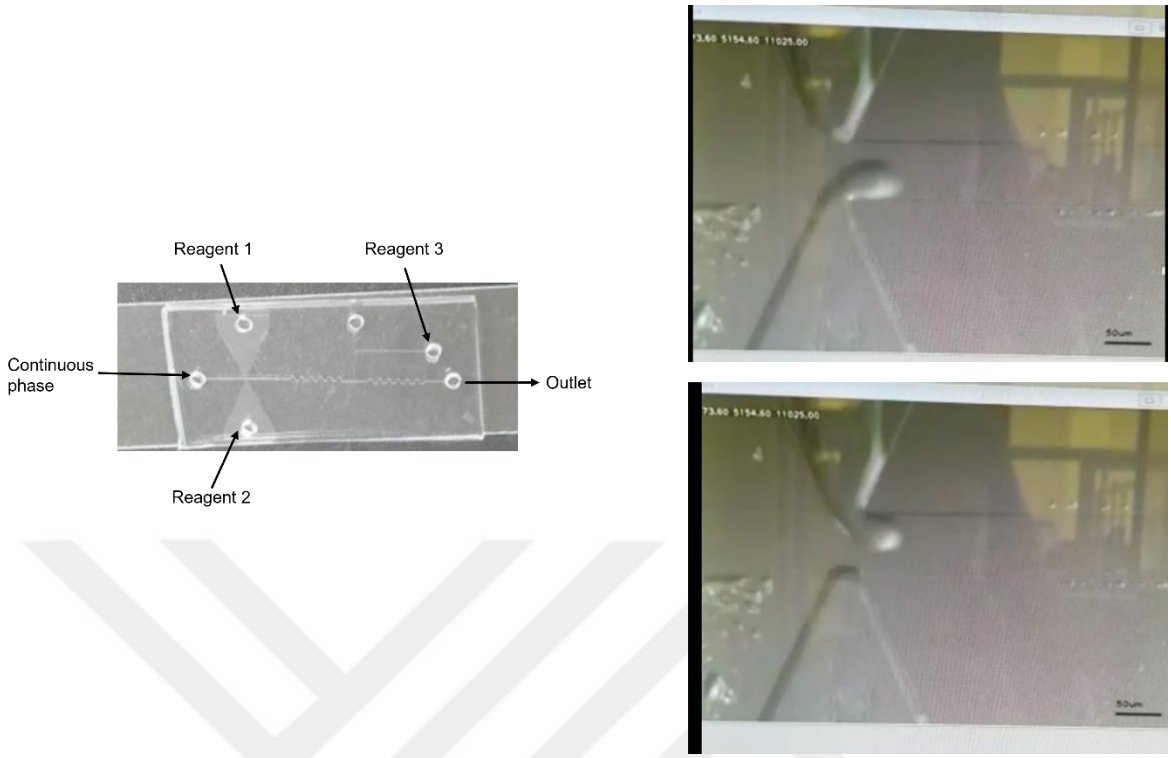


Figure 3.3 Microfluidic PDMS device and microreactor channels.

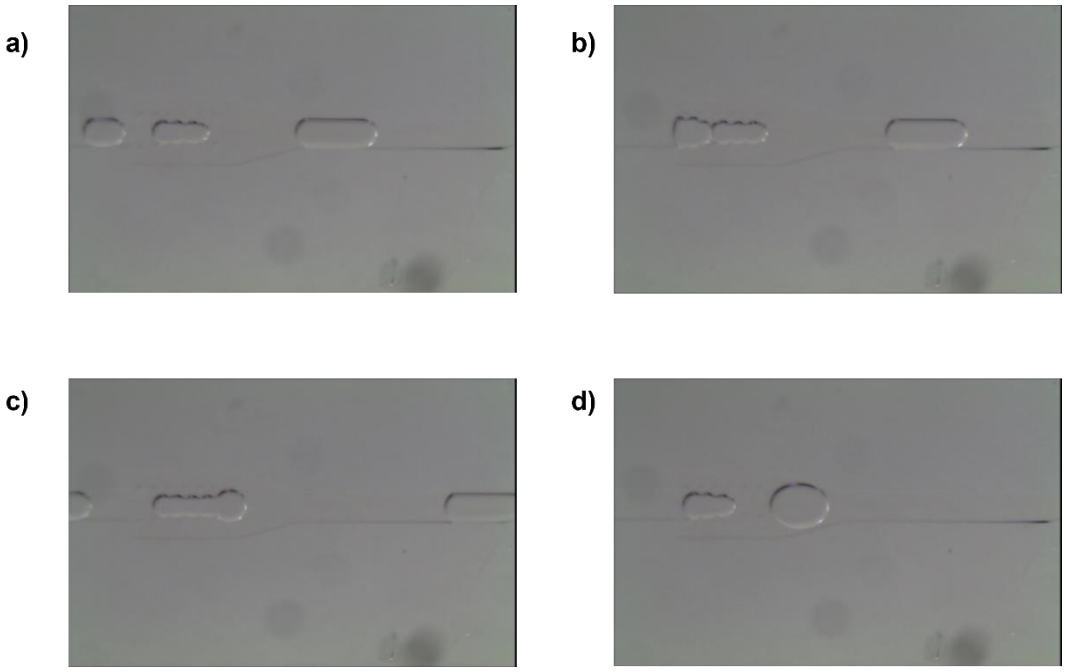


Figure 3.4 **a)** Droplet of iron chloride solution and chitosan solution in the pillar

structure before merging, **b)** and **c)** Merging of iron chloride droplet and chitosan droplet, **d)** After merging of these droplets in the pillar structure, iron-chitosan complex formed.

3.4 Characterization of SPIONs and Ch – SPIONs

3.4.1 Scanning Electron Microscopy (SEM)

Particle morphology of SPIONs and Ch – SPIONs were investigated using FEI Nova Nano SEM 430 microscope (Brno, Czech Republic). 20 kV accelerating voltage was employed during image procurement. Prior to SEM imaging, a thin layer of gold coating was applied onto samples using Quorum SC7640 high-resolution sputter coater to create an electrically conductive pathway.

3.4.2 Transmission Electron Microscopy (TEM)

Internal structures of SPIONs and Ch – SPIONs were observed using cryo – transmission electron microscopy (CTEM) in bright field and selected area diffraction (SAED) modes (FEI TECNAI F30). Before analysis, both particles were dispersed in 2-propanol, 1µl of each solution was dropped on holey carbon coated copper grid and allowed to dry for 5 minutes.

3.4.3 X-ray Diffraction (XRD)

Crystallographic information of the SPIONs and Ch – SPIONs were obtained by Rigaku D/Max-2200 X-ray diffractometer (Tokyo, Japan) using monochromatic Cu Kα radiation ($\lambda = 1.54$ Å) at 40 kV and diffraction angles (2θ) from 10 ° to 90 ° were scanned with 2 °/min scanning rate.

3.4.4 Fourier Transform Infrared Spectrometer (FTIR)

Chemical bonds present for the SPIONs and Ch – SPIONs nanoparticles were analyzed using Perkin Elmer 400 Fourier transform infrared spectrometer (Waltham, Massachusetts) preparing KBr pellets. The scanning range was 4000-400 cm^{-1} with 4 cm^{-1} scanning rate.

3.4.5 Vibrating Sample Magnetometer (VSM)

300 mg of SPIONs and Ch – SPIONs were analyzed using Cryogenic Limited PPMS vibrating sample magnetometer. Both powders were packed in capsule container and their magnetization values were measured in the applied field range of -1 T to 1 T at 298 K.

3.4.6 Thermogravimetric Analysis (TGA)

10 mg of dried specimens were heated at a rate of 10 °C/min under nitrogen atmosphere and analysis was carried out using TA Instruments SDT 650. Mass loss of SPIONs and Ch – SPIONs were plotted as percentage against temperature (100-600 °C).

3.4.7 Osteoblast Cell Interaction with SPIONs and Ch – SPIONs

To evaluate the bone cell interactions of the particles, osteoblasts (hFOB, ATCC-CRL 11372, passage number 11) were cultured using growth medium (DMEM supplemented with 10% fetal bovine serum (FBS), 1 % penicillin-streptomycin and 1 % L-glutamine under standard cell culture conditions (5 % CO_2 at 37 °C). Before the experiment, SPIONs and Ch – SPIONs were sterilized with 70 % (v / v) of ethanol and UV light. Osteoblasts were seeded at a density of 20.000 cells/cm^2 and cultured for 24 h. Afterwards, media containing different concentrations of SPIONs,

and Ch – SPIONs were added onto cells and incubated up to 7 days in vitro. To assess the cytotoxicity of the particles, colorimetric analysis was performed using MTT assay. At 1st, 3rd, 5th and 7th days of culture, media was aspirated, and samples were washed with 1xPBS. 125 µL of 3-(4,5-dimethyl-2-thiazolyl)-2,5-diphenyl-2H-tetrazolium bromide (MTT) solution was added into each well and incubated for 4 h to form formazan crystals. To dissolve the formazan crystals, 125 µL of 2-propanol-HCl solution was added to the wells. The optical density at 570 nm was measured using a Thermo Scientific Multiskan GO spectrophotometer. For magnetically stimulated samples, experiment was conducted at the same density of cells and same incubating conditions. The only difference was that cells were cultured and incubated under magnetic field up to 7 days in vitro. The experiment was conducted three times and three replicates were run each time.

3.4.8 Antibacterial Properties of SPIONs and Ch – SPIONs

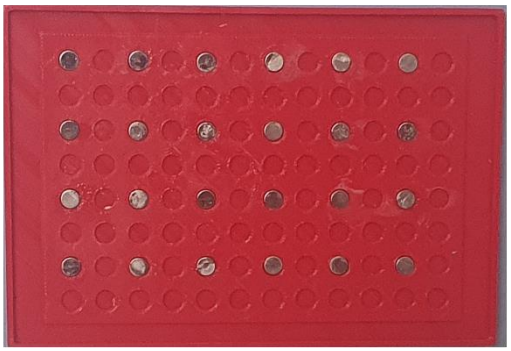
Before the experiments samples were sterilized with 70 % (v/v) ethanol and UV light. *Staphylococcus aureus* (*S. aureus*) (ATCC 25923) and *Pseudomonas aeruginosa* (*P. aeruginosa*) (ATCC 27853) were used to assess antibacterial properties. Tryptic soy broth (TSB) was used as a culture media. The bacteria were streaked onto tryptic soy agar (TSA) plates to form colonies for 24 h. After 24 h, a single colony was taken from the agar plate and inoculated in 3 % (w/v) TSB and cultured for 18 h at 200 rpm. The density of the bacteria solution was adjusted with 1xPBS to reach 0.5 in McFarland scale [42]. 100 µL of nanoparticle solution and 100 µl of diluted bacteria solution were seeded into 96-well plates to give 10 g/L, 5 g/L, 1 g/L, 0.5 g/L, 0.1 g/L, 0.05 g/L, and 0.01 g/L concentrations. The particles interacted with bacteria for 12, 24, and 48 h. During incubation, both magnetic plates and non-magnetic plates were used to investigate the influence of magnetization on bacteria. At these time points, the cultured sample solutions were diluted with 1xPBS up to 5 logs and seeded on sterile TSA plates. Seeded plates were incubated at 35 °C for 24 h and the colonies were counted. For the biofilm experiments, a similar

procedure was followed. Bacteria solution adjusted to be at 0.5 in McFarland scale was added into 96-well plates and incubated for 24 h to form a biofilm. After this step, the medium was discarded and 200 µL of TSB containing nanoparticles was added to the biofilms. To understand the interaction of bacteria and magnetic nanoparticles under a magnetic field, magnetic plates were used after nanoparticles onto biofilms. After 24 h incubation period, TSB was gently discarded. 200 µl of 0.1 % (w/v) crystal violet (CV) dye was added to each well and incubated for 15 min. Subsequently, each well was washed with 1xPBS and air dried in the dark room. To dissolve CV, 99 % (v/v) ethanol was put into each well and incubated for 15 min. The optical density at 600 nm was recorded using Thermo Scientific Multiskan GO spectrophotometer. The experiment was done three times with each at least four samples.

3.4.9 Magnetic Field Simulation

For cell culture and antibacterial assay, a magnetic plate was printed and the magnetic field strength within the individual well was computed using a stationary solver in COMSOL Multiphysics version 5.5. As shown in Figure 3.5 and Figure 3.6, a 3D model of the plate was used with 24 permanent magnets placed under the wells as a 4x6 grid with 18mm center-to-center distances, leaving an empty well along both directions. The permanent magnets were N35 grade, with 5.06 mm diameter and 1.02 mm thickness. The magnetic field strength in the sample containers placed within the wells were computed.

a)



b)

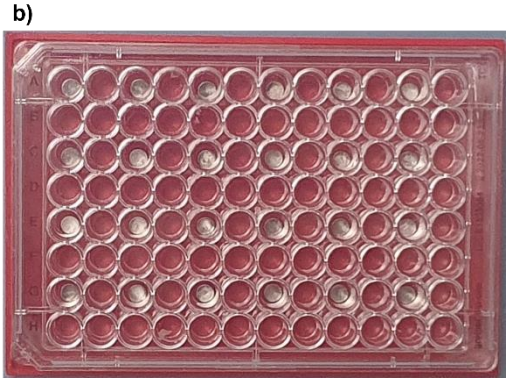


Figure 3.5 **a)** 3-D printed magnetic plate and **b)** magnetic plate system which was used for biological tests.

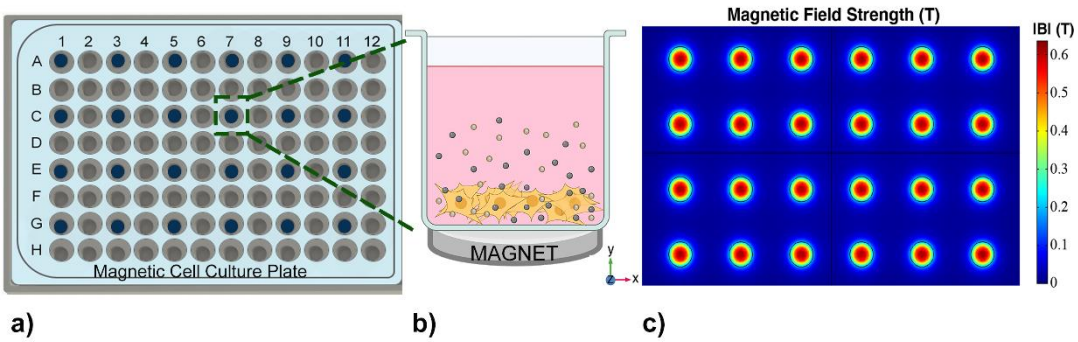


Figure 3.6 Schematic representation of **a)** magnetic cell culture plate that used for cell viability assay and antibacterial test, **b)** osteoblast cells with SPIONs (black particles) and with Ch – SPIONs (orange particles) under magnetic field, **c)** Magnetic field strength of neodymium magnets, which were used to produce magnetic field for cell culture and antibacterial assay in x, y, and z directions.

3.4.10 MRI Contrast Agent Performance

SPIONs reduce both the relaxation times of T_1 and T_2 of the surrounding medium, with increasing SPIONs concentrations causing a greater reduction. Magnetic resonance contrast performance is measured through relaxivities r_1 and r_2, which quantify the reduction in relaxation times for the unit concentration of the contrast agent. Accordingly, larger r_1 and r_2 indicate better performance as MRI contrast agent. Typically for SPIONs, the reduction in T_2 has a more significant effect than the reduction in T_1. As a result, SPIONs typically reduce the MRI signal around them, demonstrating a negative contrast effect.

To evaluate their contrast agent performance, the relaxivities r_1 and r_2 of Ch – SPIONs were measured on a 3 T magnetic resonance imaging scanner (Siemens Magnetom Trio) using a 32-channel head coil. For these experiments, a series of Ch – SPIONs were prepared in 1.5 mL vials at 7 different iron concentrations: C = [0.68

1.37 2.05 2.74 4.10 5.47 6.84] mM, as shown in Figure 3.7. For measuring r_1, a turbo spin echo inversion recovery sequence was utilized, and T_1-weighted imaging was performed at 12 different inversion times (TI) ranging between 24-1900 ms, with TR/TE = 2000/12 ms. For measuring r_2, a single echo spin echo sequence was utilized, and T_2-weighted imaging was performed at 12 different echo times (TE) ranging between 10-800 ms, with TR = 3000 ms. Other imaging parameters that were kept common for these two sequences were 12x12 cm^2 FOV, and 4 mm slice thickness. The acquisition matrix was 256x256 for T_1-weighted imaging and 128x102 for T_2-weighted imaging.

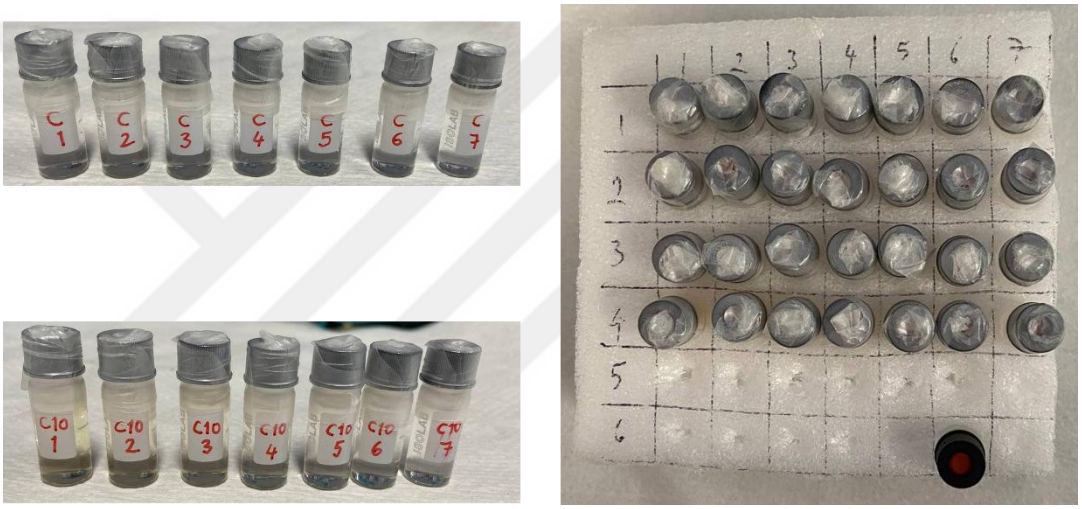


Figure 3.7 Seven different iron concentration of Ch – SPIONs which were used in MR imaging.

The images were analyzed using an in-house MATLAB (Mathworks, Natick, MA) script. A fixed size region of interest (ROI) was drawn and placed over the relevant image region of each vial. First, the T_1 value for each sample at each TI was determined using the following inversion recovery equation:

$$S=S_0(1-2^{e^{-TI/T_1}}+e^{-TI/T_1})$$

Likewise, the T_2 value for each sample at each TE was determined using the following mono exponential decay equation:

$$S=S_0 e^{-TE/T_2}$$

To determine r_1 and r_2, the inverses of T_1 and T_2 as functions of concentration were fitted to linear curves, respectively:

$$\frac{1}{T_1}=\frac{1}{T_{1,0}}+r_1 C$$

$$\frac{1}{T_2}=\frac{1}{T_{2,0}}+r_2 C$$

Here, r_1 and r_2 are the slopes of the linear fits corresponding to the relaxavities, and $T_{1,0}$ and $T_{2,0}$ are the y-intercepts of the fits corresponding to the relaxation times of the medium in the absence of Ch – SPIONs.

3.4.11 Statistical Analysis

The results were calculated as mean ± standard deviation. statistical analysis was carried out with ANOVA using Tukey's post-hoc test with significance based on $*p \leq 0.05$ in SPSS software.

CHAPTER 4

RESULTS AND DISCUSSION

SPIONs and Ch – SPIONs were synthesized using a multistep microfluidic procedure shown in the Figure 4.1 in microfluidic system. During synthesis of these nanoparticles, silicon oil was used as a continous phase to break down the dispersed phase, namely iron salt solution and chitosan solution, droplets formed in the channel. Each droplet of iron solution and chitosan solution were merged at the pillar structure as shown in previous section in Figure 3.4. A droplet of ammonia solution was then merged into this mixture of iron chloride and chitosan solution to undergo a reaction. Formed nanoparticles collected outlet of the device. The device properties which affect particle size, particle formation, their biological interaction with osteoblast cells, *S. aureus*, *P. aeruginosa*, and MRI contrast performance were individually examined under the following headings.

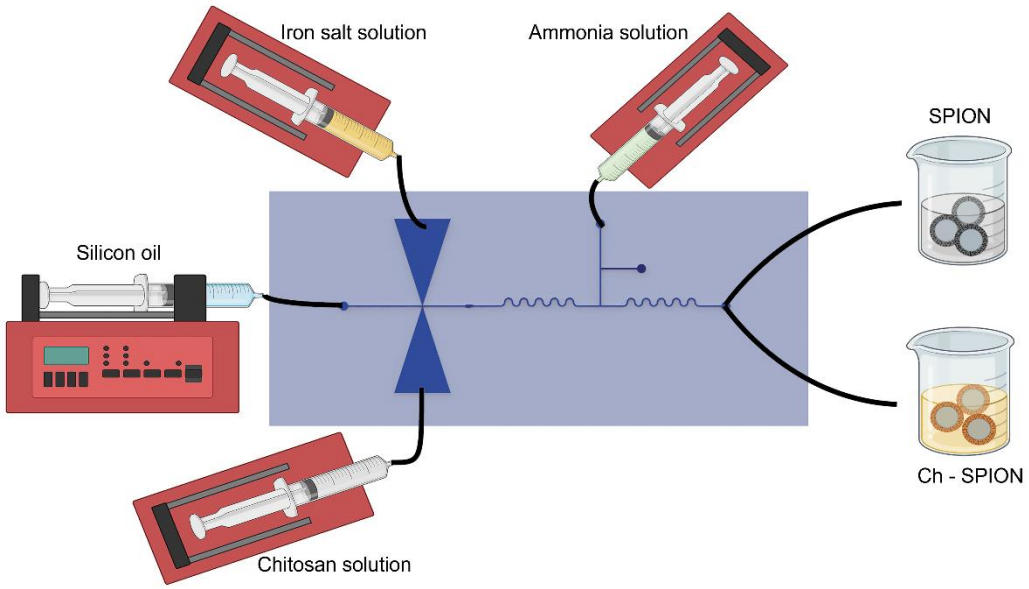


Figure 4.1 Microfluidic synthesis procedure of both SPIONs and Ch – SPIONs .

4.1 Synthesis of SPIONs and Ch – SPIONs

To synthesize SPIONs and Ch – SPIONs, PDMS microreactor was fabricated using soft lithography. The flow rate of continuous phase (silicon oil) affects the size of droplets of dispersed phase. Droplets of iron chloride and chitosan solutions merged in the pillar. Pillar in the microfluidic channel provided the expansion of the width of channel from 150 μm to 350 μm, formed dispersed phase droplets slowed down and merged. When these droplets merged in the pillar, Fe^{2+} and Fe^{3+} ions captured by amino groups of chitosan and chitosan – iron complex formed [42]. Due to this chelating effect, the chitosan layer acted as a controller of the crystallite size of iron core [42]. Since the Fe – chitosan complex formed before nucleation, this complex controlled iron ion diffusion during the growth phase of the particles, providing a narrow size distribution and small diameter [43]. After forming Fe – chitosan complex, ammonia provides the crystallization reaction of SPIONs and Ch – SPIONs to occur, improves the homogeneity and prevents the formation of agglomerates during crystal growth. As particles formed, color change was observed in the droplets. This multi-step procedure in a microreactor gave more opportunity to control the physicochemical properties of nanoparticles and reaction kinetics during synthesis [44]–[46]. The size and shape of the synthesized nanoparticles were analyzed using SEM and TEM as shown in Figure 4.3. In SEM images, the shapes of both particles were spherical and their surface chemistry was analyzed using energy dispersive X-ray spectroscopy (EDAX). Ch – SPIONs had higher amount of carbon element (34.56 % wt.) than SPIONs (2.46 % wt.) ones, where the source of carbon was from the tape material on which the sample was placed. At the same time, the amount of iron element decreased from 77.38 % by weight to 39.94 % by weight as shown in Figure 4.3. Because the synthesized particles had very small size and outstanding magnetization, the clear shape and size distribution of them were investigated using CTEM. Based on the images obtained, the average diameters of the SPIONs were 6.8 ± 0.6 nm, while the average diameters of the Ch – SPIONs were 8.8 ± 1.2 nm, as shown in Table 4.1. When obtained particle sizes were

analyzed, SPIONs and Ch – SPIONs had uniform size distribution with average size range 8.8 ± 1.2 nm. The suspension of SPIONs in water or in ethanol was unstable and these nanoparticles agglomerated approximately 60 minutes due to the highly attractive forces, which were Van Der Waals and the magnetic dipole forces between the nanoparticles, stabilization of SPIONs and Ch – SPIONs nanoparticles was shown in Figure 4.2 [13]. Since SPIONs did not have charge on their surfaces at pH = 6 – 8, they had a tendency to agglomerate in aqueous medium at neutral pH [54], [55]. However, coating SPIONs with chitosan provided additional surface charge to SPIONs, and thus induced both electrostatic and steric repulsion between nanoparticles in medium [56], [57] . So, chitosan layer provides stabilization of SPIONs for long time and Ch – SPIONs ones showed better stability in medium for MRI application. The thermal stability of SPIONs and Ch – SPIONs was investigated up to 600 °C with thermogravimetric analysis, as shown in Figure 4.4c. When SPIONs heated from 25 °C to 600 °C, first, physically, and chemically bond water occurred between 25 °C – 200 °C. Then, the conversion of magnetite to maghemite occurred between 200 °C – 300 °C, further phase transformation of the SPIONs occurred between 300 °C – 600 ° C. Obtained results are in line with the findings of literature [58]. Based on the TGA curves, Ch – SPIONs also had three decomposition stages; the first occurred between 25 ° C and 156 °C, the second occurred between 156 ° C and 400 ° C, and the third occurred between 400 °C – 600 °C [59]. In the first stage, the mass loss of chitosan was approximately 7.2 % by weight due to the removal of adsorbed water. In the second stage, decomposition of chitosan took place with a total mass loss of 26.1 % wt. due to the deacetylation of chitosan and cleavage of glycoside bonds via dehydration and deamination [59]–[61]. Weight loss after 400 ° C could be explained by the thermal devastation of the pyranose ring, which resulted in the production of formic acid and butyric acid [61]. While total weight loss of Ch – SPIONs was nearly 30.4 %, while the weight loss of SPIONs was nearly 11.9 %. Since Ch – SPIONs had a higher amount of weight loss than SPIONs, TGA results further confirmed the presence of a considerable amount of chitosan on the surfaces of SPIONs.

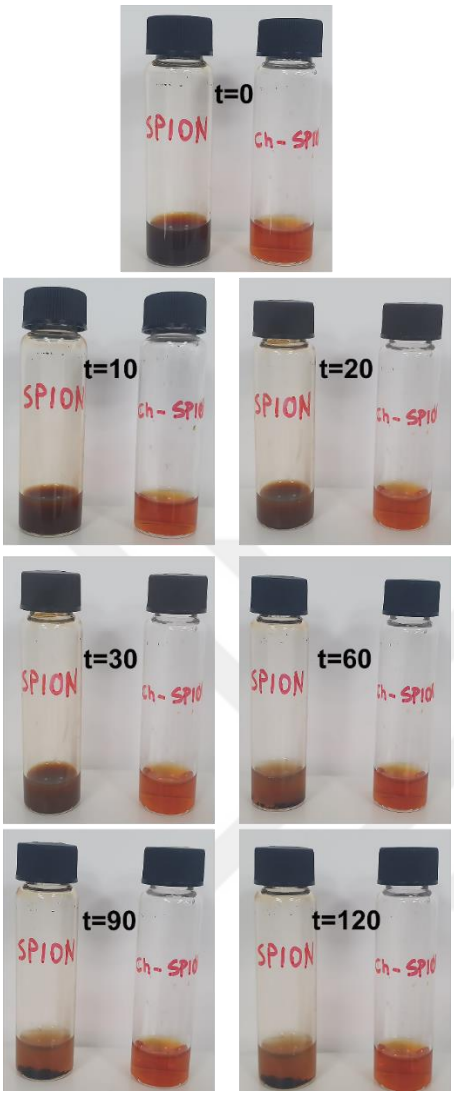


Figure 4.2 Aggregation behavior of SPIONs and Ch – SPIONs at different points, t=0, 10, 20, 30, 60, 90, 120 minutes.

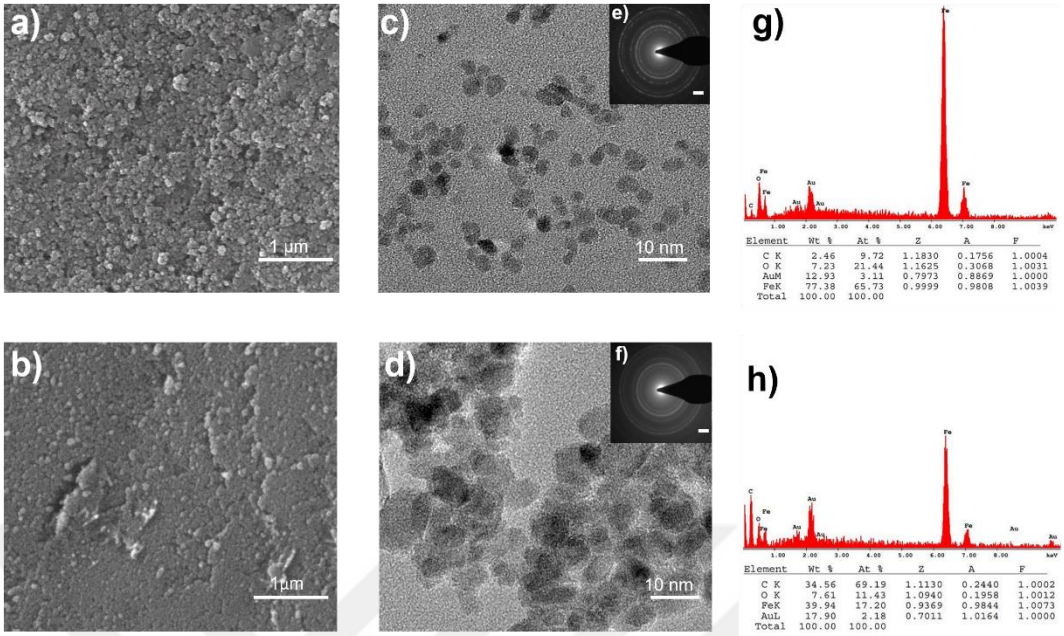


Figure 4.3 SEM and TEM images of **a**,**c)** SPIONs, **b**,**d)** Ch – SPIONs . Diffraction pattern of **e)** SPIONs and **f)** Ch – SPIONs . EDX of **g)** SPIONs and **h)** Ch – SPIONs.

Table 4.1 The size and zeta potentail of both SPIONs and Ch – SPIONs

	Size (nm)	Zeta Potential (mV)
SPIONs	6.80±0.55	-19.77±1.06
Ch - SPIONs	8.78±1.23	23.7±0.55

To investigate the crystal structure of both nanoparticles, XRD diffractogram was analyzed and it was shown in Figure 4.4a. The observed peaks of SPIONs were at 2θ = 30.25°, 35.58°, 43.17°, 53.46°, 57.13°, 62.72°, 70.96°, 74.08°, 79.32° and 87.11°(JCPDS – 19-0629) [62]. These peaks were in agreement with the standard pattern of spinel-shaped crystalline magnetite [56], [62]. For Ch – SPIONs , the relative intensities of characteristic peaks changed but chitosan coating did not affect the crystalline structure of magnetite.

SPIONs and Ch – SPIONs were characterized using FTIR spectra to understand their absorption bands of them in 4000 – 500 cm^{-1} as shown in Figure 4.4b. Both SPIONs

and Ch – SPIONs had a peak at around 572 cm^{-1}, which was the Fe-O stretching vibration of the the tetrahedral sites of spinel structure [63]. This peak confirmed the presence of Fe_3O_4 in Ch - SPIONs. The peak at 872 cm^{-1} was Fe – O stretching vibration, which was only found in SPIONs. The peaks 1383 cm^{-1} and 1058 cm^{-1} were stretching vibrations of the -CO-CN- and ether group of C-O in chitosan, respectively [63]–[65] . The peaks at 3429 and 1627 cm^{-1} were stretching and bending of the OH group of water that was adsorbed by the nanoparticles [66].

The superparamagnetic behaviour of SPIONs and Ch – SPIONs were analyzed using VSM. When synthesized nanoparticles are small enough, they demonstrate superparamagnetic behaviour [67]. For biomedical application, this behaviour is preferred because their remnant magnetization is zero when external magnetization is removed [68], [69]. This implies that these nanoparticles do not agglomerate or cause clogging in the blood stream due to the absence of coercive force or remnance [70]. The magnetization behavior of synthesized both nanoparticles is shown in Figure 4.4d, the magnetization saturation of SPIONs and Ch – SPIONs were 54.82 emu/g and 31.98 emu/g, respectively. Both had a superparamagnetic nature, yet Ch – SPIONs particles had lower magnetization value due to the coating layer.

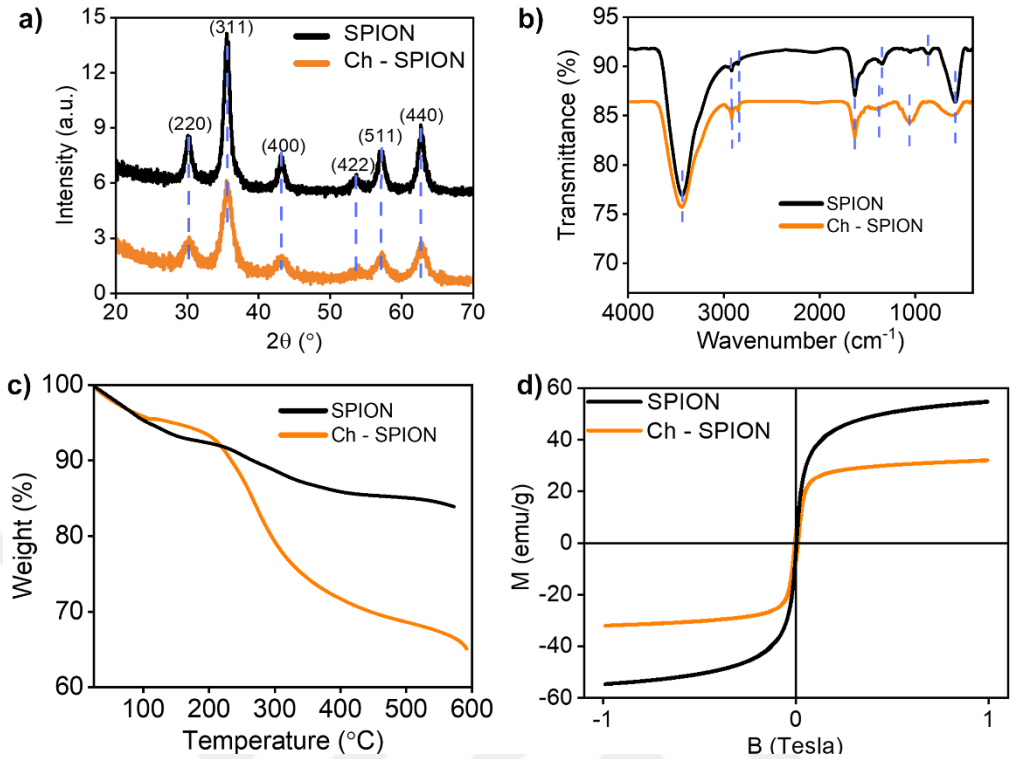


Figure 4.4 **a)** XRD graph **b)** FTIR spectra **c)** TGA gravimetric diagram **d)** VSM graph of SPIONs and Ch – SPIONs .

4.2 Osteoblast Interaction of SPIONs and Ch – SPIONs

MTT assay was used to measure cell viability of osteoblast cells with SPIONs and Ch – SPIONs nanoparticles (particle concentration: 10 g/L, 5 g/L, 1 g/L, 0.5 g/L, 0.1 g/L). Both SPIONs and Ch – SPIONs nanoparticles interacted with osteoblast cells for up to 7 days. As a control sample, cells were seeded in 96-well plates and were well grown up to 7 days without nanoparticles. Five different concentrations of SPIONs and Ch – SPIONs cultured into the 96-well plates. For both types of DMEM with nanoparticles, the highest concentration of them had the lowest optical density. While decreasing the concentration of DMEM with nanoparticles, cell proliferation increased (Figure 4.5 – Figure 4.6). Ch – SPIONs samples had less viable cells than SPIONs samples. MTT test was carried out in the absence and in the presence of an external static magnetic field. Up to 0.5 g/L concentration, cell proliferation

promoted at 1st, 3rd ,5th and 7th days. However, at high concentration of nanoparticles, cell proliferation decreased due to the high surface area to volume ratio, composition, surface coating and overall charge [71].

The interaction between nanoparticles and cells also depends on the size, concentration, and synthesis method [72]. Each effect on various cells specifically osteoblast cells was examined in this section. Nanoparticles with small size provide the internalization through the cells easily and size designates the level of toxicity on cells. Elbakry *et al.* explained that smaller size (20 nm) can easily penetrate CHO-K1 and HeLa cells compare to larger particle sizes (30, 50, 80 nm) [73]. Additionally, nanoparticles of smaller size leads to more interaction areas that might induce cytotoxicity. For example, gold nanoparticles having 1.4 nm size showed greater toxicity on cells at 30 μM – 56 μM while particles of 15 nm size were nontoxic at 60 – fold higher concentration [74]. Therefore, SPIONs had a higher mass toxicity in osteoblast cells [75]. In addition, toxicity of SPIONs depends on concentration of particles. A study stated that low concentration of nanoparticles (20 μg/mL) promoted osteoblast cells while high concentration (> 200 μg/mL) decreased the cell proliferation [72]. Thus, our study showed that osteoblast cell proliferation increased when particle concentration decreased from 1 g/L to 0.1 g/L concentration. Other factors which effect the internalization of SPIONs through cells are coating, surface charge of synthesized particles. Chitosan coating ensured the stability of produced particles, while at the same time the cell membrane of osteoblast cells showed higher permeability to Ch – SPIONs because of the positive charge on the chitosan layer [76]. Chitosan which was used in this study had low molecular weight (50-190 kDa) and high acetylation degree (75-85 %), thus Ch – SPIONs caused lower osteoblast cells proliferation compared to SPIONs. In Figure 4.5, Ch – SPIONs nanoparticles had half of osteoblast proliferation compared to SPIONs.

For the experiments conducted in the absence of external magnetic field (Figure 4.5a and 4.5c), results showed that hFOBs successfully proliferated up to 7 days in vitro upon the interaction with nanoparticles independent of the presence of chitosan and particle concentration. For both SPIONs and Ch – SPIONs , the highest nanoparticle

concentration exhibited the lowest viability of hFOBs. Decreasing the concentration of the nanoparticles increased cellular viability in a dose-dependent manner. Interestingly, SPIONs promoted higher viability of hFOB than Ch – SPIONs . Similar trends were also observed when hFOB – nanoparticle interactions occurred in the presence of an external static magnetic field (Figures 4.5b and 4.5d). Both SPIONs and Ch – SPIONs showed dose-dependent hFOB viability [72] . Although hFOB proliferation was promoted for SPIONs in the presence of magnetic field for all nanoparticle concentrations up to 7 days, high Ch – SPIONs concentrations (10 g/L) compromised hFOB viability. At 3rd day, hFOB cell viability increased 5 times at 10g/L of SPIONs concentration in the presence of magnetic field compared to hFOB which were cultured in the absence of magnetic field. At the lowest concentration of Ch – SPIONs (0.1 g/L), cell viability of hFOB 1.2 times increased in the presence of magnetic field when compared to absence of magnetic field. Furthermore, on day 7th, hFOB cell viability increased 1.5 times at a concentration of Ch – SPIONs of 0.1 g/L in the presence of magnetic field when compared to hFOB which were cultured in the absence of a magnetic field (Figure 4.5). Thus, the presence of a magnetic field increased the viability of the hFOB up to 7 days for both nanoparticles. Figures 4.7 (a-d) showed the hFOB morphologies in the presence and absence of an external static magnetic field. We observed that hFOBs which were interacted with SPIONs and Ch – SPIONs are well spread and appeared healthy.

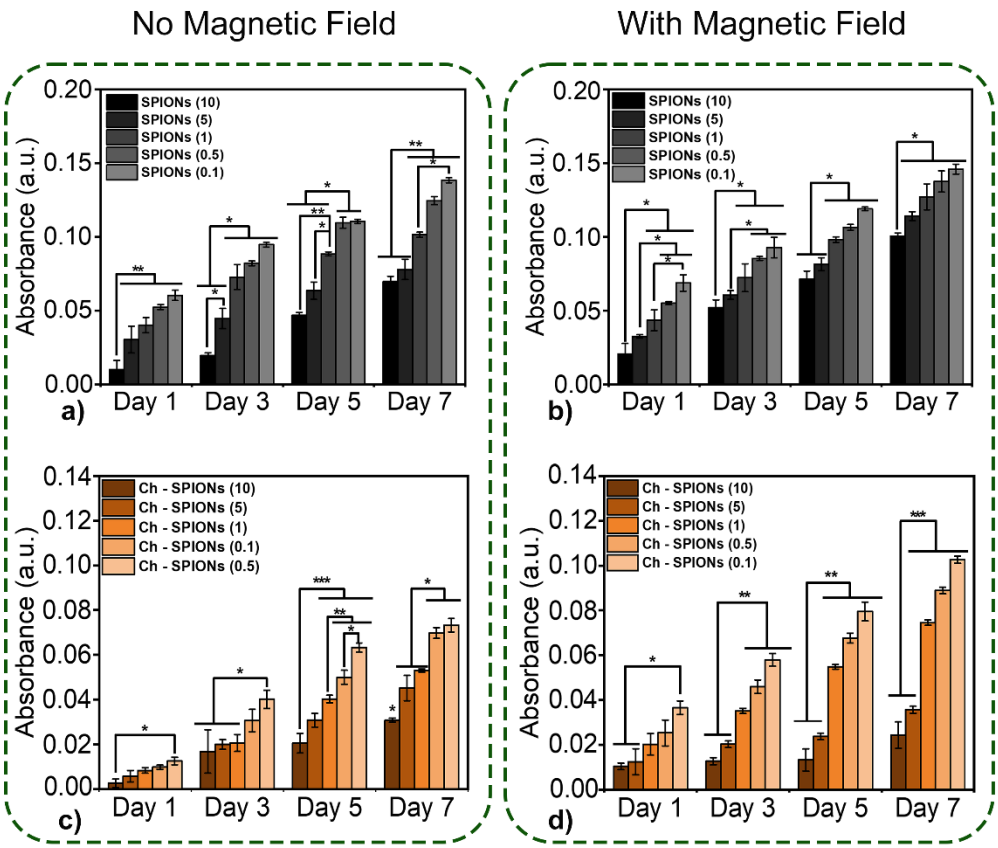


Figure 4.5 Osteoblast (hFOB) cells proliferation without magnetic field for **a)** SPIONs and **c)** Ch – SPIONs , with magnetic field for **b)** SPIONs and **d)** Ch – SPIONs up to 7 days. Values are mean ± SD (n=3), *p< 0.05, **p< 0.01, ***p< 0.005.

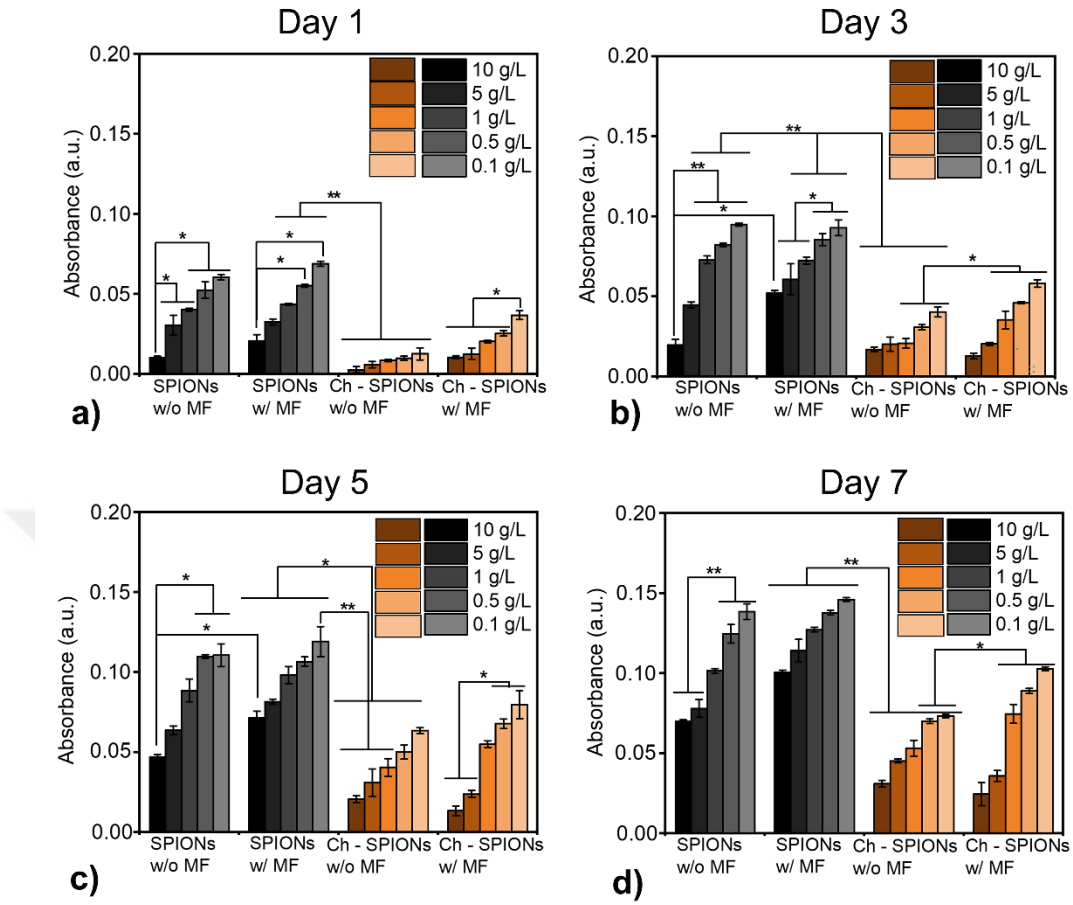


Figure 4.6 Comparison of hFOB proliferation in the absence and in the presence of magnetic field at 10, 5, 1, 0.5, 0.1 g/L of concentration for **a)** day 1, **b)** day 3, **c)** day 5, and **d)** day 7. Values are mean ± SD (n=3), **p*< 0.05, ***p*< 0.01.

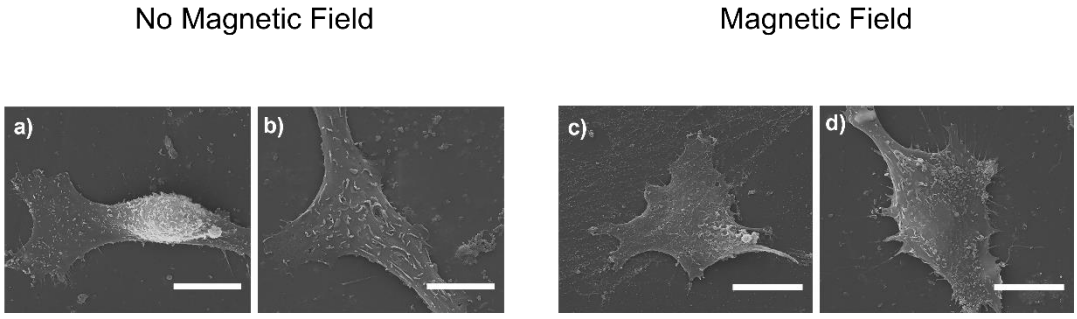


Figure 4.7 SEM images of hFOB cells on nanoparticles **a)** SPIONs, **b)** Ch – SPIONs in the absence of magnetic field, **c)** SPIONs and **d)** Ch – coated SPIONs in the presence of magnetic field. Scale bars are 20 μm.

4.3 Antibacterial Properties of SPIONs and Ch – SPIONs

The antibacterial test was performed with *S. aureus* and *P. aeruginosa* bacteria. The diluted bacteria solution at a density of 0.5 McFarland [77] and 0.3 % (v/v) concentration of TSB with nanoparticles were seeded in a 96-well plate at the same time for the colony count assay which was performed at three different time points which were 12, 24 and 48 h (Figure 4.8 and Figure 4.9). Both SPIONs and Ch-SPIONs nanoparticles had an antibacterial activity compared to control samples that had no particles. Ch – SPIONs and SPIONs interacted with magnetic and no magnetic plates during incubation for all time points. Results showed that both SPIONs and Ch – SPIONs, independent of the presence of a chitosan, had an antibacterial activity compared to control samples which had no nanoparticles. All concentrations of SPIONs and Ch – SPIONs led to a significant reduction in the number of colonies against both *P. aeruginosa* and *S. aureus* after 12, 24, and 48h. Similar to the cytotoxicity experiments, concentration-dependent decrease in bacteria growth was observed in both strains for both SPIONs and Ch – SPIONs. The colony growth of *S. aureus* decreased by 52 %, and of *P. aeruginosa*, colony growth was decreased by 47% compared to TCPS control which had no nanoparticles for 48 h in the absence of magnetic field. The antibacterial effect of nanoparticles these bacteria strains could be explained with surface charge – based attraction between the nanoparticles and the bacteria. The positively charged Ch – SPIONs was observed to destroy the negatively charged bacterial strains due to electrostatic attraction [78]. Electrostatic interaction might cause the production of reactive oxygen species (ROS) for both SPIONs and Ch – SPIONs [3], [29], [79]. To produce a high amount of ROS, a higher nanoparticle concentration and stronger nanoparticle-bacteria interaction can be used in the antibacterial assay. When Ch –

SPIONs interacted with both bacteria strains, they were shown to generate higher amounts of radical formation than the SPIONs due to formation of oxidative stress [80]. In the absence of magnetic field, Ch – SPIONs showed better antibacterial property for all concentrations for all time points. For example, Ch – SPIONs decreased the number of *S. aureus* colonies by 57 % while SPIONs decreased the number of colonies by 22 % at 0.01 g/L of concentration for 12 h. Furthermore, Ch – SPIONs decreased the number of colonies of *S. aureus* by 93 % while SPIONs decreased the number of colonies by 80 % at 10 g/L concentration for 24 h. In the case of *P. aeruginosa*, in the absence of a magnetic field, Ch – SPIONs decreased the number of colonies by 35 % while SPIONs decreased the number of *P. aeruginosa* colonies by 23 % at 0.01 g/L of concentration for 12 h. For 48 h, Ch – SPIONs decreased the number of *P. aeruginosa* colonies 47 % when compared to TCPS control, which had no nanoparticles. Thus, Ch – SPIONs showed better antibacterial activity against *S. aureus* for 12 h, 24 h in the absence of magnetic field. In the presence of magnetic field (Figure 4.9), all experimental concentrations of Ch – SPIONs led to approximately 1-log reduction in the number of colonies against both *P. aeruginosa* and *S. aureus* after 12, 24, and 48 h. For *S. aureus* and *P. aeruginosa* bacteria colonies were shown in Figure 4.10. Similar to bacteria growth results in the absence of magnetic field, concentration dependent decrease in bacteria growth was observed for both strains upon their interaction with SPIONs and Ch – SPIONs in the presence of magnetic field. *S. aureus* decreased by 53 % for 48 h, and the colony growth of *P. aeruginosa* decreased by 41 % for 24 h compared to absence of magnetic field. It is important to note that the decrease in bacteria colonies was much more significant in the presence of a magnetic field. For instance, when *S. aureus* interacted with Ch – SPIONs in the absence of magnetic field, the number of colonies was decreased by 57 % when compared to TCPS control samples at 0.1 g/L of concentration for 12 h. However, in the presence of magnetic field, the number of colonies of *S. aureus* decreased by 82 % when compared to TCPS control at 0.1 g/L of concentration for 12 h. In the case of *P. aeruginosa*, Ch – SPIONs caused a 9-fold reduction in the presence of magnetic field compared to in the absence of magnetic

field at 0.01 g/L of concentration for 48 h. Additionally, Ch – SPIONs decreased the *P. aeruginosa* colony growth by 95 % at 10 g/L of concentration for 12 h when compared to TCPS control. Thus, the influence of external static magnetic field was more pronounced for *S. aureus* than *P. aeruginosa*. For instance, Ch – SPIONs decreased the *S. aureus* growth rate by 53 %, while it decreased the *P. aeruginosa* growth rate by 25 % at 0.01 g/L of concentration for 48 h. Although there are a few studies on the use of static magnetic fields in antibacterial tests, Kamel *et al.* stated that the presence of a magnetic field interfered with the surface charge of the bacterial membrane [81]. Additionally, the effect of the presence of static magnetic field on bacterial strains can be explained three mechanisms which are ion interference mechanism, free radical theory, and membrane theory [82]. Based on these three theories, the static magnetic field can change the binding state of the ion – protein complex or produce free radicals that are deadly for bacteria macromolecules or cause molecular rotation in the bacterial membrane due to the presence of diamagnetic anisotropy molecules [82]. This molecular rotation influences the ion channels and ion mobility in bacteria [82]. The enhanced decrease in bacteria colonies was likely caused by bacterial membrane disruption due to combination of magnetic field with nanoparticles. Since magnetic field created more openings on the bacterial cell wall, higher number of nanoparticles could enter bacteria and the antibacterial activity enhanced [83].

The growth of *P. aeruginosa* and *S. aureus* after their interaction with all concentrations (10, 5, 1, 0.5, 0.1, 0.05, 0.01 g/L) of SPIONs and Ch – SPIONs were tested with CV staining. Nanoparticles interacted with *S. aureus* and *P. aeruginosa* in the presence and in the absence of magnetic field as shown in Figure 4.11(a-d). When both nanoparticles were tested with *S. aureus*, Ch – SPIONs were observed to decrease existing biofilm more than the SPIONs. For instance, *S. aureus* biofilm mass was decreased by 46 % at concentration of 10 g/L when compared to control sample. Furthermore, although *S. aureus* was interacted with the lowest concentration of nanoparticles (0.01 g/L), Ch – SPIONs decreased by 30 % when compared to control which did not have nanoparticles. When both nanoparticles

interacted with *P. aeruginosa*, they both reduced biofilm growth compared to nanoparticle free bacteria controls. Importantly, when nanoparticles were compared to each other, Ch – SPIONs were observed to be more effective than the SPIONs. For instance, Ch – SPIONs decreased the existence of *P. aeruginosa* biofilm mass by 70 % in the absence of magnetic field at a concentration of 5 g/L while SPIONs decreased biofilm mass by 62 % compared to control. Although the lowest concentration (0.01 g/L) of Ch – SPIONs were used against *P. aeruginosa*, the biofilm mass was decreased by 19 % in the absence of magnetic field when compared to the control. The inhibitory effect of nanoparticles on the existing biofilms of *P. aeruginosa* and *S. aureus* could be correlated with size and shape of nanoparticles together with electrostatic interaction. In the presence of magnetic field, Ch – SPIONs showed 25 % loss of biofilm formation against *P. aeruginosa* for each tested concentration when compared to absence of magnetic field. Furthermore, Ch – SPIONs caused *S. aureus* biofilm by 46 % when compared to the control. At 0.001 g/L of Ch – SPIONs concentration, the reduction in the mass of the *S. aureus* biofilm was decreased by 31 % when compared to the control. To decrease the existence biofilm mass, nanoparticles should penetrate bacteria [3]. Xu et al. studied the change in thickness of the *S. aureus* biofilm mass under a magnetic field [84]. The presence of a magnetic field provided a deeper penetration into the biofilm mass, since *S. aureus* caused an acidic environment, nanoparticles degraded, and ions caused bacteria to die [84].

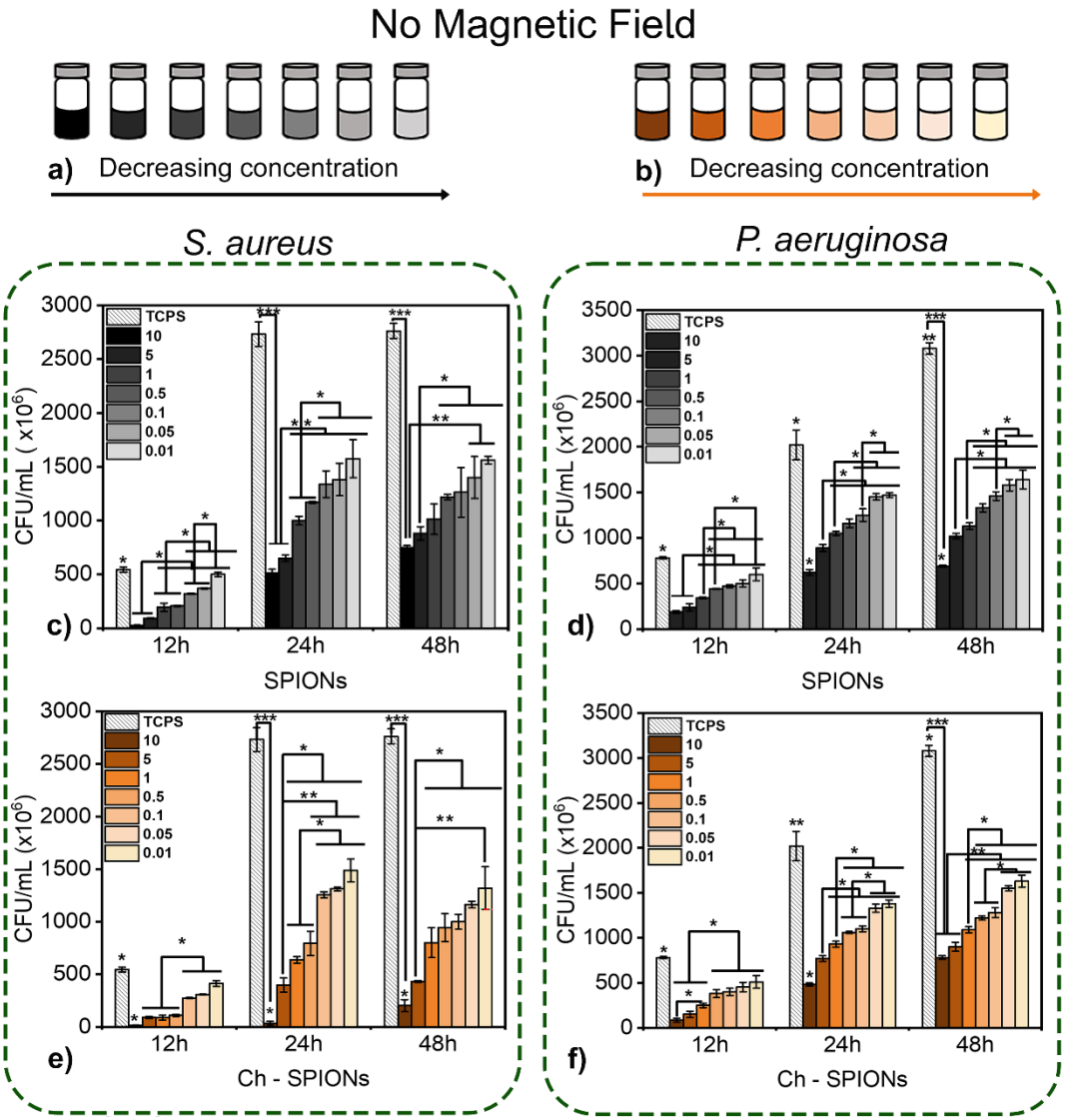


Figure 4.8 Schematic representation of seven different concentrations of TSB with **a)** SPIONs (black) and **b)** Ch – SPIONs (orange) without magnetic field. Number of colonies for SPIONs against **c)** *S. aureus*, **d)** *P. aeruginosa* and Ch – SPIONs against **e)** *S. aureus*, **f)** *P. aeruginosa* at seven different concentrations for 12, 24 and 48 h were shown. Values are mean ± SD (n=3), **p*< 0.05, ***p*< 0.01, ****p*< 0.005.

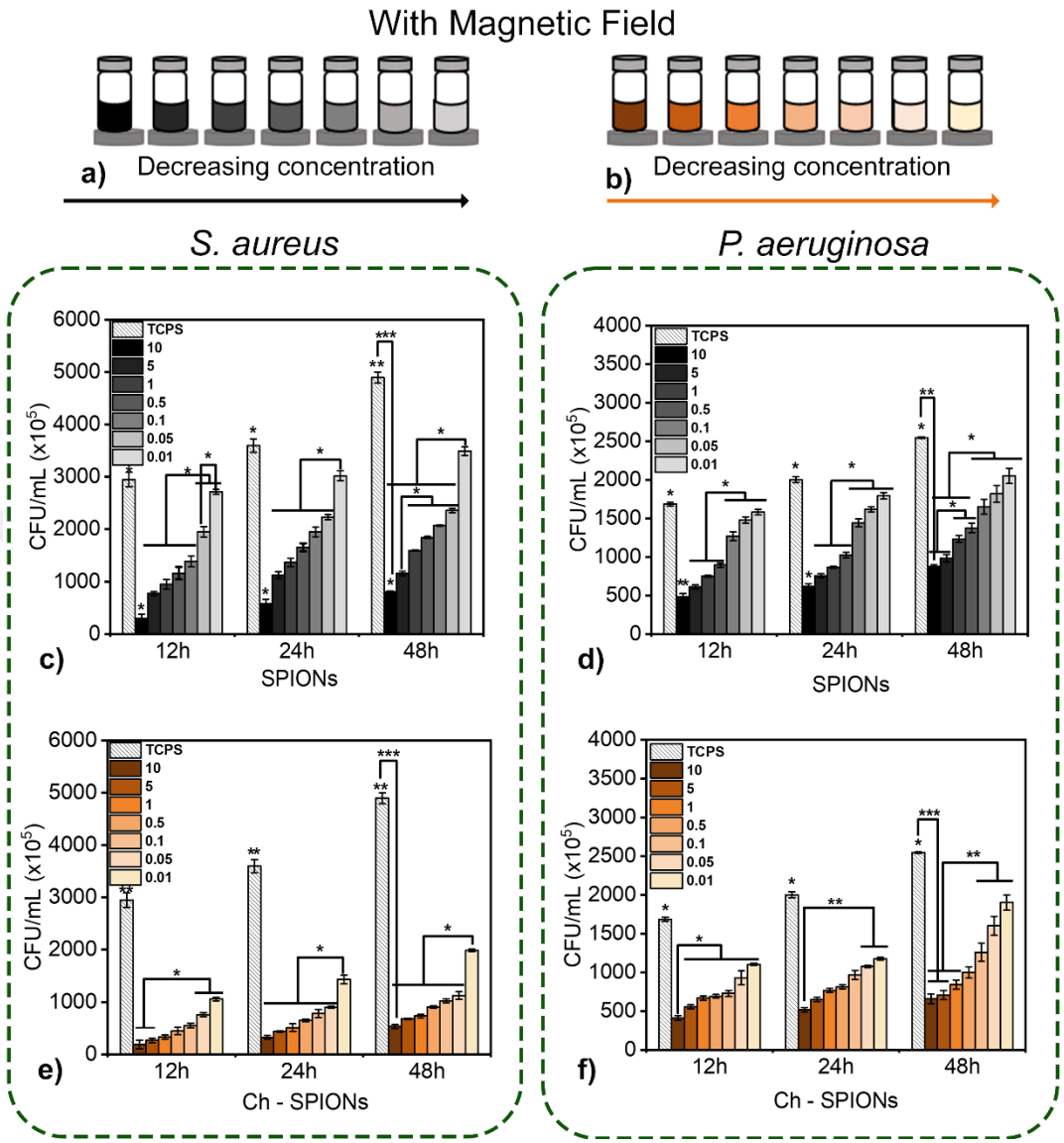


Figure 4.9 Schematic representation of seven different concentrations of TSB with **a)** SPIONs (black) and **b)** Ch – SPIONs (orange) with magnetic field. Number of colonies for SPIONs against **c)** *S. aureus*, **d)** *P. aeruginosa* and Ch – SPIONs against **e)** *S. aureus*, **f)** *P. aeruginosa* at seven different concentrations for 12, 24 and 48 h were shown. Values are mean ± SD (n=3), *$p< 0.05$, **$p< 0.01$, ***$p< 0.005$.

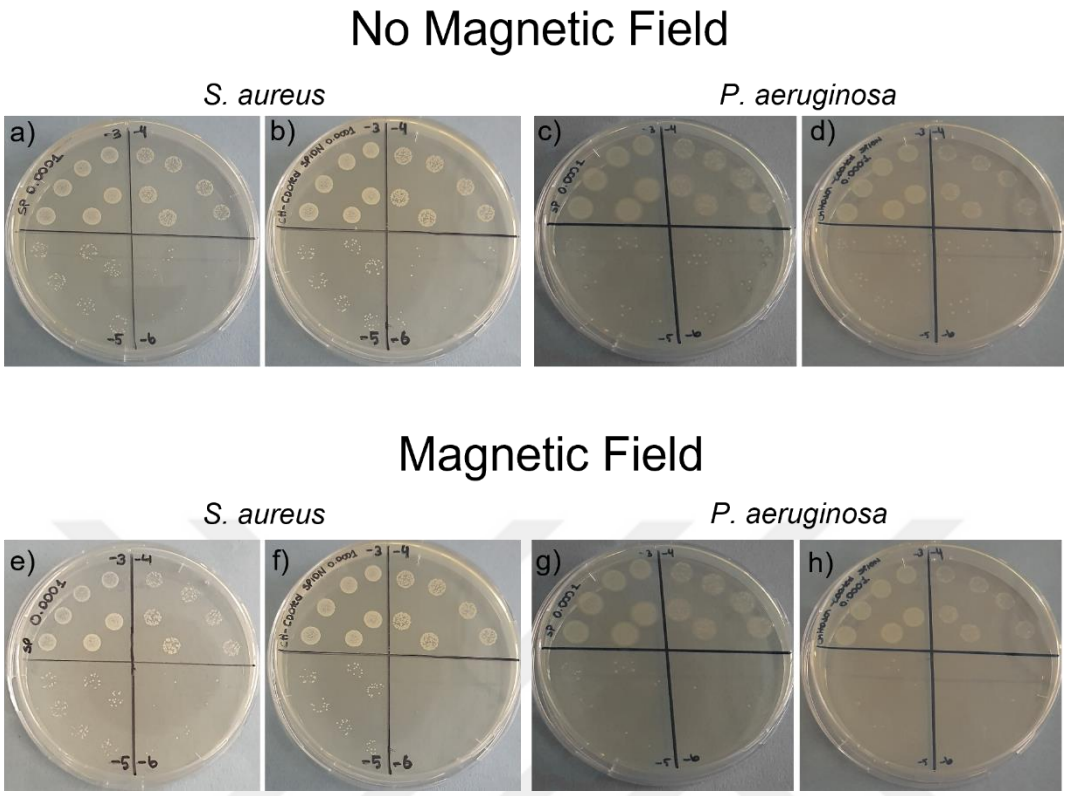


Figure 4.10 *S. aureus* colonies with **a)** SPIONs, **b)** Ch – SPIONs at and *P. aeruginosa* colonies with **c)** SPIONs, **d)** Ch – SPIONs and *S. aureus* colonies with **e)** SPIONs, **f)** Ch – SPIONs at and *P. aeruginosa* colonies with **g)** SPIONs, **h)** Ch – SPIONs at 0.0001 mg/mL concentration growing on agar plate with magnetic field.

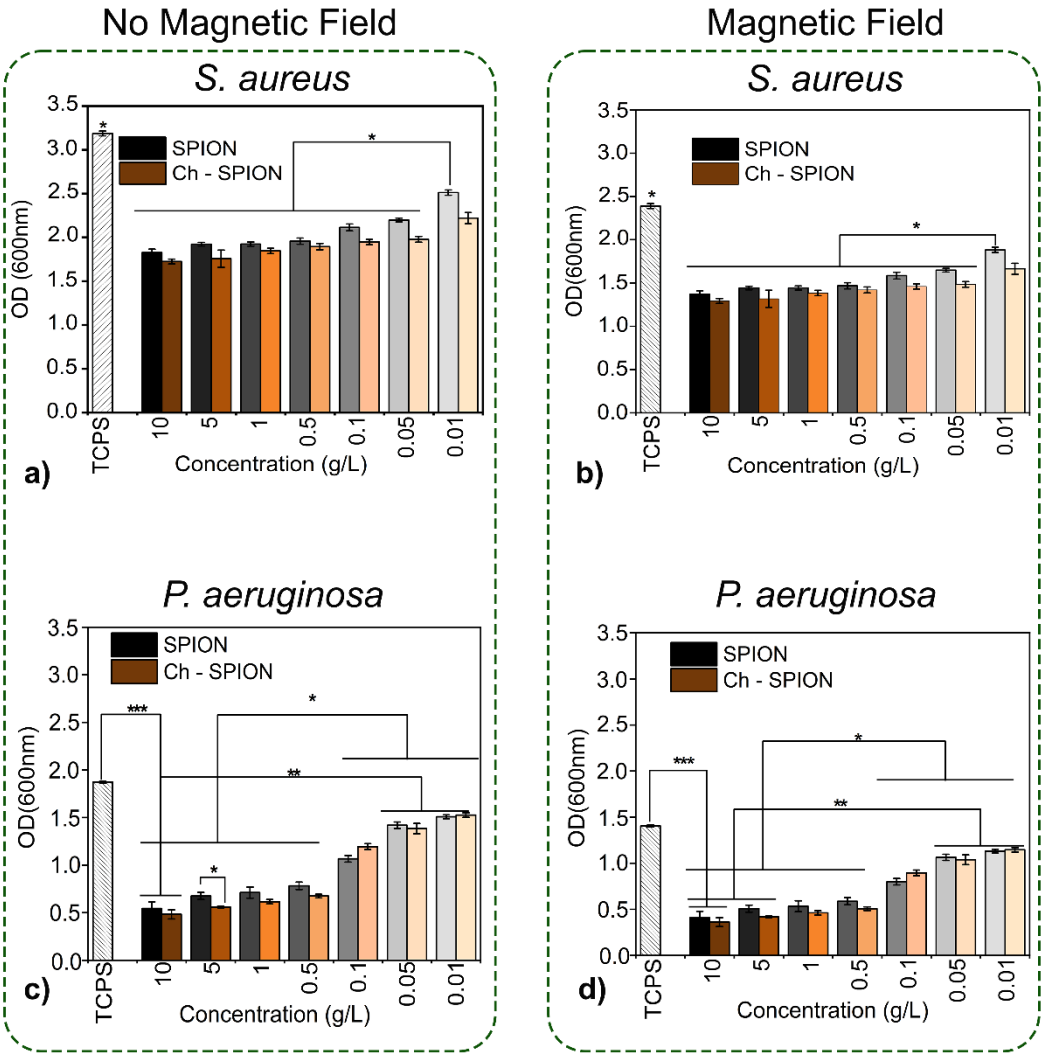


Figure 4.11 Biofilm assay performed for all concentrations of SPIONs and Ch – SPIONs up to 24 h without magnetic field against **a)** *S. aureus* and **b)** *P. aeruginosa* and with magnetic field against **c)** *S. aureus* and **d)** *P. aeruginosa*. Values are mean ± SD (n=3), **p*< 0.05.

4.4 MRI Contrast Performance of Synthesized Nanoparticles

MRI contrast performance evaluations for Ch – SPIONs are displayed in Figure 4.12, together with example T_1- and T_2-weighted MRI images. According to the linear fits in Figure 4.12, the relaxivities measured at 3 T for Ch – SPIONs were r_1

= 0.428 mM^{-1} s^{-1} and r_2 = 7.764 mM^{-1} s^{-1}. Similar experiments were also performed for SPIONs. However, due to their colloidal instability in water, SPIONs immediately agglomerated at the bottom of the vials, rendering MRI relaxivity measurements impractical. In contrast Ch – SPIONs displayed good colloidal stability at various concentrations, as reflected by the small error bars and excellent linear fits in Figure 4.12 These results show that Ch – SPIONs have relatively high r_2 relaxivities comparable to those in the literature [85] , and a moderate-to-low r_1 relaxivity. Therefore, Ch – SPIONs is dominantly acting as negative contrast agents in MRI, providing improved visibility by reducing the MRI signal of the tissues around them.

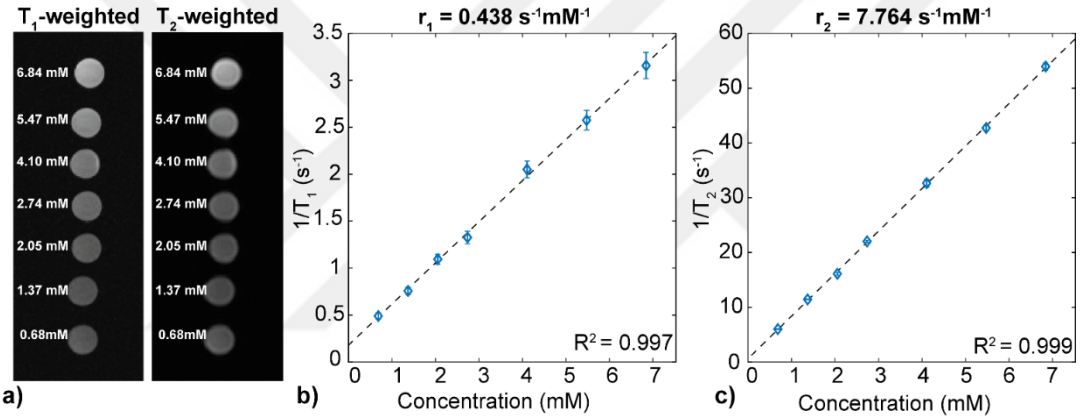


Figure 4.12 **a)** Example T_1-weighted and T_2-weighted MRI images at 3 T. Measured relaxivities were **b)** r_1 = 0.428 mM^{-1} s^{-1} and **c)** r_2 = 7.764 mM^{-1} s^{-1} for Ch – SPIONs at 3 T. Graphics display the change in the inverse of T_1 and T_2 relaxation times as a function of iron concentration, for C= [0.68, 1.37, 2.05, 2.74, 4.10, 5.47, 6.84] mM. The error bars designated mean and standard deviation relaxation rates over all pixels in ROIs, dashed line showed linear fit to all data points.

CONCLUSION AND FUTURE WORK

The destruction of biofilm is crucial for the treatment of infection. Since bacteria gained resisstance to commnly-used antibacterial agents, the usage of antibacterial nanoparticles against bacterial infection can be a new strategy. Novel properties of nanoparticles include their magnetization behaviour, physical and biological features. This thesis has explained the synthesis of SPIONs and Ch-SPION nanoparticles using microfluidic channels to assess their antibacterial properties and use them as a contrast agent in MRI. Since amino groups of chitosan captured the iron ions during syntehsis of Ch - SPIONs, small nanoparticles formed. Using a microreactor during both SPIONs and Ch – SPIONs synthesis provided control on the reaction kinetics and physicochemical properties of the nanoparticles. While the size of SPIONs was 6.8 ± 0.6 nm, the size of Ch – SPIONs particles were 8.8 ± 1.2 nm. SPIONs did not stabilize in aqueous medium because they had highly attractive Van der Walls and magnetic dipole forces, so they agglomerated. However, Ch – SPIONs were stabile in the medium. Thus, Ch – SPIONs can be used as a contrast agent in magnetic resonance imaging.

The toxicity of synthesized SPIONs and Ch-SPIONs has been studied with osteoblast cells in the presence and absence of external static magnetic field. Though cells proliferated up to 7 days under both condition, SPIONs had higher number of viable cells than Ch – SPIONs, potentially due to the degree of acetylation and molecular weight of chitosan which affected cytocompatibility of the nanoparticles. In addition, minimal effect was observed in cell viability upon the application of magnetic field.

The antibacterial activity of the nanoparticles was studied against *S. aureus* and *P. aeruginosa* strains in the presence and absence of a magnetic field. Ch – SPIONs showed better antibacterial activity against both gram positive and gram negative

strains due to the polycationic surface charge and the small size of the nanoparticles. When Ch – SPIONs showed up to 5 – fold reduction at 0.001 concentration of nanoparticles at 48 h against both bacteria strains under magnetic field, they showed up to 2 – fold decreased in colonies at the sam condition in the absence of a magnetic field during incubation. Additionally, Ch – SPIONs decreased 25 % of biomass against both bacteria for 24 h under magnetic field compared to no magnetic condition.

The MRI contrast agent performance of the SPIONs was measured on a 3 T MRI scanner. Ch – SPIONs successfully acted as a negative contrast agent in MRI and displayed good colloidal stability.

Thus, synthesized Ch – SPIONs nanoparticles in a microreactor were successful candidates as an antibacterial agent to destroy existing biofilm and contrast agent for MRI application.

Apart from these findings, there are some points that should be improved with further research.

- Although microfluidics provide better mass transfer and control over nanoparticles, some aspects device fabrication should be improved. For instance, during making of the PDMS device, delamination might occur if PDMS did not bond appropriately to the glass slide. Delamination during synthesis caused leakage of the dispersed phase solution which leads to non-effective particle synthesis [86].
- The small diameter of the microreactor channel also causes a clogging problem during particle synthesis [87]. Clogging might cause channel blockage [88], [89] and this effect is stronger on the wall side of the channel due to the laminar flow profile [90].
- During synthesis of nanoparticles, when flow rates of dispersed and continuous phases are not optimized, burst delamination is also occurred. This may result in experimental failure. Additionally, production rate of

polymeric solution is also limited due to the microfluidic system dimensions [86], [88].

- Although many studies stated that chitosan is a biocompatible polymer, this depends on acetylation and molecular weight of chitosan. Biocompatibility of Ch – SPIONs might be improved using low degree of acetylation and high molecular weight chitosan during synthesis [91].
- In vivo experiments can be designed to assess the efficacy of Ch – SPIONs to target and fight with infection.

REFERENCES

[1] E. M. Materón, C. M. Miyazaki, O. Carr, N. Joshi, P. H. S. Picciani, C. J. Dalmaschio, F. Davis, F. M. Shimizu, "Magnetic nanoparticles in biomedical applications: A review," *Applied Surface Science Advances*, vol. 6, 2021, doi: 10.1016/j.apsadv.2021.100163.

[2] N. Hoshyar, S. Gray, H. Han, and G. Bao, "The effect of nanoparticle size on in vivo pharmacokinetics and cellular interaction," *Nanomedicine*, vol. 11, no. 6, pp. 673–692, 2016, doi: 10.2217/nnm.16.5.

[3] A. B. Seabra, M. T. Pelegrino, and P. S. Haddad, *Antimicrobial Applications of Superparamagnetic Iron Oxide Nanoparticles: Perspectives and Challenges*. Elsevier Inc., 2017. doi: 10.1016/B978-0-323-46152-8.00024-X.

[4] N. Ajinkya, X. Yu, P. Kaithal, H. Luo, P. Somani, and S. Ramakrishna, "Magnetic iron oxide nanoparticle (Ionp) synthesis to applications: Present and future," *Materials*, vol. 13, no. 20, pp. 1–35, 2020, doi: 10.3390/ma13204644.

[5] A. G. Niculescu, C. Chircov, A. C. Bîrcă, and A. M. Grumezescu, "Nanomaterials synthesis through microfluidic methods: An updated overview," *Nanomaterials*, vol. 11, no. 4, 2021, doi: 10.3390/nano11040864.

[6] D. Liu, S. Cito, Y. Zhang, C. F. Wang, T. M. Sikanen, and H. A. Santos, "A versatile and robust microfluidic platform toward high throughput synthesis of homogeneous nanoparticles with tunable properties," *Advanced*

Materials, vol. 27, no. 14, pp. 2298–2304, 2015, doi: 10.1002/adma.201405408.

[7] S. K. Y. Tang and G. M. Whitesides, "Basic Microfluidic and Soft Lithographic Techniques," pp. 7–32.

[8] S. Damiati, U. B. Kompella, S. A. Damiati, and R. Kodzius, "Microfluidic devices for drug delivery systems and drug screening," *Genes (Basel)*, vol. 9, no. 2, 2018, doi: 10.3390/genes9020103.

[9] H. Wei, Y. Hu, J. Wang, X. Gao, X. Qian, and M. Tang, "Superparamagnetic iron oxide nanoparticles: Cytotoxicity, metabolism, and cellular behavior in biomedicine applications," *Int J Nanomedicine*, vol. 16, no. May, pp. 6097–6113, 2021, doi: 10.2147/IJN.S321984.

[10] M. K. Khalid, M. Asad, P. Henrich-Noack, M. Sokolov, W. Hintz, L. Grigartzik, E. Zhang, A. Dityatev, B. van Wachem, and B. A. Sabel, "Evaluation of toxicity and neural uptake in vitro and in vivo of superparamagnetic iron oxide nanoparticles," *Int J Mol Sci*, vol. 19, no. 9, pp. 1–14, 2018, doi: 10.3390/ijms19092613.

[11] H. Wei, Y. Hu, J. Wang, X. Gao, X. Qian, and M. Tang, "Superparamagnetic iron oxide nanoparticles: Cytotoxicity, metabolism, and cellular behavior in biomedicine applications," *Int J Nanomedicine*, vol. 16, no. July, pp. 6097–6113, 2021, doi: 10.2147/IJN.S321984.

[12] C. L. Meisel, P. Bainbridge, R. V. Mulkern, D. Mitsouras, and J. Y. Wong, "Assessment of superparamagnetic iron oxide nanoparticle poly(ethylene glycol) coatings on magnetic resonance relaxation for early disease detection," *IEEE Open J Eng Med Biol*, vol. 1, no. May, pp. 116–122, 2020, doi: 10.1109/OJEMB.2020.2989468.

[13] M. Mahmoudi, S. Sant, B. Wang, S. Laurent, and T. Sen, "Superparamagnetic iron oxide nanoparticles (SPIONs): Development,

surface modification and applications in chemotherapy," *Adv Drug Deliv Rev*, vol. 63, no. 1–2, pp. 24–46, 2011, doi: 10.1016/j.addr.2010.05.006.

[14] G. Unsoy, S. Yalcin, R. Khodadust, and P. Mutlu, "IN SITU SYNTHESIS and CHARACTERIZATION OF CHITOSAN COATED IRON OXIDE NANOPARTICLES and LOADING OF DOXORUBICIN," no. October, 2012.

[15] Wahajuddin and S. Arora, "Superparamagnetic iron oxide nanoparticles: Magnetic nanoplatforms as drug carriers," *Int J Nanomedicine*, vol. 7, pp. 3445–3471, 2012, doi: 10.2147/IJN.S30320.

[16] A. Gholami, F. Mohammadi, Y. Ghasemi, N. Omidifar, and A. Ebrahiminezhad, "Antibacterial activity of SPIONs versus ferrous and ferric ions under aerobic and anaerobic conditions: A preliminary mechanism study," *IET Nanobiotechnol*, vol. 14, no. 2, pp. 155–160, 2020, doi: 10.1049/iet-nbt.2019.0266.

[17] W. Duszynska, V. D. Rosenthal, A. Szczesny, K. Zajaczkowska, M. Fulek, and J. Tomaszewski, "Device associated –health care associated infections monitoring, prevention and cost assessment at intensive care unit of University Hospital in Poland (2015–2017)," *BMC Infect Dis*, vol. 20, no. 1, Dec. 2020, doi: 10.1186/s12879-020-05482-w.

[18] M. Kolpa, M. Walaszek, A. Gniadek, Z. Wolak, and W. Dobroś, "Incidence, microbiological profile and risk factors of healthcare-associated infections in intensive care units: A 10 year observation in a provincial hospital in southern Poland," *Int J Environ Res Public Health*, vol. 15, no. 1, Jan. 2018, doi: 10.3390/ijerph15010112.

[19] R. O. Darouiche, "Device-Associated Infections: A Macroproblem that Starts with Microadherence," 2001. [Online]. Available: https://academic.oup.com/cid/article/33/9/1567/1746437

[20] D. G. Maki, S. M. Stolz, S. Wheeler, and L. A. Mermel, “Annals of Internal Medicine Prevention of Central Venous Catheter-Related Bloodstream Infection by Use of an Antiseptic-Impregnated Catheter A Randomized, Controlled Trial,” 1997. [Online]. Available: http://annals.org/

[21] B. L. Robert Barrack, W. H. Harris, and B. Massachusetts, “The Value of Aspiration of the Hip Joint before Revision Total Hip Arthroplasty*.”

[22] M. J. Wilhelm, C. Schmid, D. Hammel, S. Kerber, H. M. Loick, M. Herrmann, H. H. Scheld, “Cardiac Pacemaker Infection: Surgical Management With and Without Extracorporeal Circulation,” 1997.

[23] H. Schachter, “4.06 Glycobiology of Caenorhabditis elegans.”

[24] Y. Zheng, L. He, T. K. Asiamah, and M. Otto, “Colonization of medical devices by staphylococci,” *Environmental Microbiology*, vol. 20, no. 9. Blackwell Publishing Ltd, pp. 3141–3153, Sep. 01, 2018. doi: 10.1111/1462-2920.14129.

[25] E. A. Masters, B. F. Ricciardi, K. L. de M. Bentley, T. F. Moriarty, E. M. Schwarz, and G. Muthukrishnan, “Skeletal infections: microbial pathogenesis, immunity and clinical management,” *Nature Reviews Microbiology*, vol. 20, no. 7. Nature Research, pp. 385–400, Jul. 01, 2022. doi: 10.1038/s41579-022-00686-0.

[26] N. G. Durmus, E. N. Taylor, K. M. Kummer, and T. J. Webster, “Enhanced efficacy of superparamagnetic iron oxide nanoparticles against antibiotic-resistant biofilms in the presence of metabolites,” *Advanced Materials*, vol. 25, no. 40, pp. 5706–5713, Oct. 2013, doi: 10.1002/adma.201302627.

[27] P. Gunawan, C. Guan, X. Song, Q. Zhang, S. S. J. Leong, C. Tang, Y. Chen, M. B. Chan-Park, M. W. Chang, K. Wang, and R. Xu, “Hollow fiber membrane decorated with Ag/MWNTs: Toward effective water disinfection and biofouling control,” *ACS Nano*, vol. 5, no. 12, pp. 10033–10040, Dec. 2011, doi: 10.1021/nn2038725.

[28] S. Liu, L. Wei, L. Hao, N. Fang, M. W. Chang, R. Xu, Y. Yang, and Y. Chen, “Sharper and faster ‘Nano darts’ kill more bacteria: A study of antibacterial activity of individually dispersed pristine single-walled carbon nanotube,” *ACS Nano*, vol. 3, no. 12, pp. 3891–3902, Dec. 2009, doi: 10.1021/nn901252r.

[29] N. Tran, A. Mir, D. Mallik, A. Sinha, S. Nayar, and T. J. Webster, “International Journal of Nanomedicine Bactericidal effect of iron oxide nanoparticles on Staphylococcus aureus,” 2010. [Online]. Available: https://www.dovepress.com/

[30] B. Gallez and H. M. Swartz, “In vivo EPR: When, how and why?,” *NMR in Biomedicine*, vol. 17, no. 5. pp. 223–225, Aug. 2004. doi: 10.1002/nbm.913.

[31] R. B. Lauffer, “Paramagnetic Metal Complexes as Water Proton Relaxation Agents for NMR Imaging: Theory and Design.”

[32] P. Caravan, J. J. Ellison, T. J. McMurry, and R. B. Lauffer, “Gadolinium(III) chelates as MRI contrast agents: Structure, dynamics, and applications,” *Chem Rev*, vol. 99, no. 9, pp. 2293–2352, Sep. 1999, doi: 10.1021/cr980440x.

[33] G. P. Yan, L. Robinson, and P. Hogg, “Magnetic resonance imaging contrast agents: Overview and perspectives,” *Radiography*, vol. 13, no. SUPPLL. 1. Dec. 2007. doi: 10.1016/j.radi.2006.07.005.

[34] J. Wahsner, E. M. Gale, A. Rodríguez-Rodríguez, and P. Caravan, “Chemistry of MRI contrast agents: Current challenges and new frontiers,” *Chemical Reviews*, vol. 119, no. 2. American Chemical Society, pp. 957–1057, Jan. 23, 2019. doi: 10.1021/acs.chemrev.8b00363.

[35] G. P. Yan, L. Robinson, and P. Hogg, “Magnetic resonance imaging contrast agents: Overview and perspectives,” *Radiography*, vol. 13, no. SUPPLL. 1. Dec. 2007. doi: 10.1016/j.radi.2006.07.005.

[36] O. Clément, N. Siauve, C. A. Cuénod, and G. Frija, “Liver imaging with ferumoxides (Feridex): fundamentals, controversies, and practical aspects.,” *Top Magn Reson Imaging*, vol. 9, no. 3, pp. 167–82, Jun. 1998.

[37] P. Reimer and T. Balzer, “Ferucarbotran (Resovist): A new clinically approved RES-specific contrast agent for contrast-enhanced MRI of the liver: Properties, clinical development, and applications,” *European Radiology*, vol. 13, no. 6. Springer Verlag, pp. 1266–1276, Jun. 01, 2003. doi: 10.1007/s00330-002-1721-7.

[38] J. Wahsner, E. M. Gale, A. Rodríguez-Rodríguez, and P. Caravan, “Chemistry of MRI contrast agents: Current challenges and new frontiers,” *Chemical Reviews*, vol. 119, no. 2. American Chemical Society, pp. 957–1057, Jan. 23, 2019. doi: 10.1021/acs.chemrev.8b00363.

[39] J. S. Weinstein, C. G. Varallyay, E. Dosa, S. Gahramanov, B. Hamilton, W. D. Rooney, L. L. Muldoon, and E. A. Neuwelt, “Superparamagnetic iron oxide nanoparticles: Diagnostic magnetic resonance imaging and potential therapeutic applications in neurooncology and central nervous system inflammatory pathologies, a review,” *Journal of Cerebral Blood Flow and Metabolism*, vol. 30, no. 1. pp. 15–35, Jan. 2010. doi: 10.1038/jcbfm.2009.192.

[40] S. Siavashy, M. Soltani, F. Ghorbani-Bidkorbeh, N. Fallah, G. Farnam, S. A. Mortazavi, F. H. Shirazi, M. H. H. Tehrani, and M. H. Hamedi, “Microfluidic platform for synthesis and optimization of chitosan-coated magnetic nanoparticles in cisplatin delivery,” *Carbohydr Polym*, vol. 265, no. April, p. 118027, 2021, doi: 10.1016/j.carbpol.2021.118027.

[41] J. Ahn, J. Ko, S. Lee, J. Yu, Y. T. Kim, and N. L. Jeon, “Microfluidics in nanoparticle drug delivery; From synthesis to pre-clinical screening,” *Advanced Drug Delivery Reviews*, vol. 128. Elsevier B.V., pp. 29–53, Mar. 15, 2018. doi: 10.1016/j.addr.2018.04.001.

[42] T. M. Freire, L. M. U. Dutra, D. C. Queiroz, N. M. P. S. Ricardo, K. Barreto, J. C. Denardin, F. R. Wurm, C.P. Sousa, A. N. Correia, P.de Lima-Neto, and P.B.A. Fechine, "Fast ultrasound assisted synthesis of chitosan-based magnetite nanocomposites as a modified electrode sensor," *Carbohydr Polym*, vol. 151, pp. 760–769, Oct. 2016, doi: 10.1016/j.carbpol.2016.05.095.

[43] Y. Wang, B. Li, Y. Zhou, and D. Jia, "In situ mineralization of magnetite nanoparticles in chitosan hydrogel," *Nanoscale Res Lett*, vol. 4, no. 9, pp. 1041–1046, 2009, doi: 10.1007/s11671-009-9355-1.

[44] L. Zhang, Q. Chen, Y. Ma, and J. Sun, "Microfluidic Methods for Fabrication and Engineering of Nanoparticle Drug Delivery Systems," *ACS Appl Bio Mater*, vol. 3, no. 1, pp. 107–120, 2020, doi: 10.1021/acsabm.9b00853.

[45] J. Wang and Y. Song, "Microfluidic Synthesis of Nanohybrids," *Small*, vol. 13, no. 18, pp. 1–19, 2017, doi: 10.1002/smll.201604084.

[46] S. Khizar, N. Zine, A. Errachid, N. Jaffrezic-Renault, and A. Elaissari, "Microfluidic-based nanoparticle synthesis and their potential applications," *Electrophoresis*, pp. 1–20, 2021, doi: 10.1002/elps.202100242.

[47] Q. Xu, M. Hashimoto, T. T. Dang, T. Hoare, D. S. Kohane, G. M. Whitesides, R. Langer, and D. G. Anderson, "Preparation of monodisperse biodegradable polymer microparticles using a microfluidic flow-focusing device for controlled drug delivery," *Small*, vol. 5, no. 13, pp. 1575–1581, Jul. 2009, doi: 10.1002/smll.200801855.

[48] J. Wang, Y. Li, X. Wang, J. Wang, H. Tian, P. Zhao, Y. Tian, Y. Gu, L. Wang, and C. Wang, "Droplet microfluidics for the production of microparticles and nanoparticles," *Micromachines*, vol. 8, no. 1. MDPI AG, Jan. 01, 2017. doi: 10.3390/mi8010022.

[49] I. Lee, Y. Yoo, Z. Cheng, and H. K. Jeong, “Generation of monodisperse mesoporous silica microspheres with controllable size and surface morphology in a microfluidic device,” *Adv Funct Mater*, vol. 18, no. 24, pp. 4014–4021, Dec. 2008, doi: 10.1002/adfm.200801093.

[50] N. J. Carroll, S. B. Rathod, E. Derbins, S. Mendez, D. A. Weitz, and D. N. Petsev, “Droplet-based microfluidics for emulsion and solvent evaporation synthesis of monodisperse mesoporous silica microspheres,” *Langmuir*, vol. 24, no. 3, pp. 658–661, Feb. 2008, doi: 10.1021/la7032516.

[51] S. Xu, Z. Nie, M. Seo, P. Lewis, E. Kumacheva, H. A. Stone, P. Garstecki, D. B. Weibel, I. Gitlin, and G. M. Whitesides, “Generation of Monodisperse Particles by Using Microfluidics: Control over Size, Shape, and Composition,” *Angewandte Chemie*, vol. 117, no. 5, pp. 734–738, Jan. 2005, doi: 10.1002/ange.200462226.

[52] D. Dendukuri, D. C. Pregibon, J. Collins, T. A. Hatton, and P. S. Doyle, “Continuous-flow lithography for high-throughput microparticle synthesis,” *Nat Mater*, vol. 5, no. 5, pp. 365–369, May 2006, doi: 10.1038/nmat1617.

[53] M. Abdul Wahab and E. Y. Erdem, “Multi-step microfludic reactor for the synthesis of hybrid nanoparticles,” *Journal of Micromechanics and Microengineering*, vol. 30, no. 8, pp. 1–10, 2020, doi: 10.1088/1361-6439/ab8dd2.

[54] M. Mahmoudi, S. Sant, B. Wang, S. Laurent, and T. Sen, “Superparamagnetic iron oxide nanoparticles (SPIONs): Development, surface modification and applications in chemotherapy,” *Adv Drug Deliv Rev*, vol. 63, no. 1–2, pp. 24–46, 2011, doi: 10.1016/j.addr.2010.05.006.

[55] R. Qiao, C. Yang, and M. Gao, “Superparamagnetic iron oxide nanoparticles: From preparations to in vivo MRI applications,” *J Mater Chem*, vol. 19, no. 35, pp. 6274–6293, 2009, doi: 10.1039/b902394a.

[56] A. Zhu, L. Yuan, and T. Liao, “Suspension of Fe3O4 nanoparticles stabilized by chitosan and o-carboxymethylchitosan,” *Int J Pharm*, vol. 350, no. 1–2, pp. 361–368, 2008, doi: 10.1016/j.ijpharm.2007.09.004.

[57] S. Thangudu, “Safe magnetic resonance imaging on biocompatible nanoformulations,” 2022, doi: 10.1039/d2bm00692h.

[58] U. S. Khan, Amanullah, A. Manan, N. Khan, A. Mahmood, and A. Rahim, “Transformation mechanism of magnetite nanoparticles,” *Materials Science-Poland*, vol. 33, no. 2, pp. 278–285, 2015, doi: 10.1515/msp-2015-0037.

[59] M. Ziegler-Borowska, D. Chełminiak, and H. Kaczmarek, “Thermal stability of magnetic nanoparticles coated by blends of modified chitosan and poly(quaternary ammonium) salt,” *J Therm Anal Calorim*, vol. 119, no. 1, pp. 499–506, 2015, doi: 10.1007/s10973-014-4122-7.

[60] Z. Yang, H. Peng, W. Wang, and T. Liu, “Crystallization behavior of poly(ε-caprolactone) / layered double hydroxide nanocomposites,” *J Appl Polym Sci*, vol. 116, no. 5, pp. 2658–2667, 2010, doi: 10.1002/app.

[61] J. B. Marroquin, K. Y. Rhee, and S. J. Park, “Chitosan nanocomposite films: Enhanced electrical conductivity, thermal stability, and mechanical properties,” *Carbohydr Polym*, vol. 92, no. 2, pp. 1783–1791, 2013, doi: 10.1016/j.carbpol.2012.11.042.

[62] S. Information, “Assembly of Magnetite Nanoparticles into Spherical Mesoporous Aggregates with a 3-D Wormhole-Like Porous Structure,” *Materials Science*, no. c, pp. 1–9, 2010.

[63] G. Zhao, J. Wang, X. Peng, Y. Li, X. Yuan, and Y. Ma, “Facile solvothermal synthesis of mesostructured Fe3O 4/chitosan nanoparticles as delivery vehicles for pH-responsive drug delivery and magnetic resonance imaging contrast agents,” *Chem Asian J*, vol. 9, no. 2, pp. 546–553, 2014, doi: 10.1002/asia.201301072.

[64] J. Z. Sun, Y. C. Sun, and L. Sun, “Synthesis of surface modified Fe3O4 super paramagnetic nanoparticles for ultra sound examination and magnetic resonance imaging for cancer treatment,” *J Photochem Photobiol B*, vol. 197, no. May, p. 111547, 2019, doi: 10.1016/j.jphotobiol.2019.111547.

[65] B. Wang, P. Zhang, G. R. Williams, C. Brandford-White, J. Quan, H. Nie, and L. Zhu “A simple route to form magnetic chitosan nanoparticles from coaxial-electrospun composite nanofibers,” *J Mater Sci*, vol. 48, no. 11, pp. 3991–3998, 2013, doi: 10.1007/s10853-013-7208-x.

[66] F. Saber Braim, N. Noor Ashikin Nik Ab Razak, A. Abdul Aziz, L. Qasim Ismael, and B. Kayode Sodipo, “Ultrasound Assisted Chitosan Coated Iron Oxide Nanoparticles: Influence of Ultrasonic Irradiation on the Crystallinity, Stability, Toxicity and Magnetization of the Functionalized Nanoparticles,” *Ultrason Sonochem*, vol. 88, no. June, p. 106072, 2022, doi: 10.1016/j.ultsonch.2022.106072.

[67] A. V. Samrot, N. Shobana, P. Durga Sruthi, and C. S. Sahithya, “Utilization of chitosan-coated superparamagnetic iron oxide nanoparticles for chromium removal,” *Appl Water Sci*, vol. 8, no. 7, Nov. 2018, doi: 10.1007/s13201-018-0841-4.

[68] S. Savliwala, A. Chiu-Lam, M. Unni, A. Rivera-Rodriguez, E. Fuller, K. Sen, M. Threadcraft, and C. Rinaldi, “Magnetic nanoparticles”. *Elsevier Inc.*, 2019. doi: 10.1016/B978-0-12-816662-8.00013-8.

[69] Y. Wei, B. Han, X. Hu, Y. Lin, X. Wang, and X. Deng, “Synthesis of Fe3O4 nanoparticles and their magnetic properties,” *Procedia Eng*, vol. 27, no. December, pp. 632–637, 2012, doi: 10.1016/j.proeng.2011.12.498.

[70] S. M. Dadfar, D. Camozzi, M. Darguzyte, K. Roemhild, P. Varvarà, J. Metselaar, S. Banala, M. Straub, N. Güvener, U. Engelmann, I. Slabu, M. Buhl, J. Leusen, P. Kögerler, B. Hermanns-Sachweh, V. Schulz, F. Kiessling, and T. Lammers, “Size-isolation of superparamagnetic iron oxide

nanoparticles improves MRI, MPI and hyperthermia performance," *J Nanobiotechnology*, vol. 18, no. 1, pp. 1–13, 2020, doi: 10.1186/s12951-020-0580-1.

[71] N. Nelson, J. Port, and M. Pandey, "Use of Superparamagnetic Iron Oxide Nanoparticles (SPIONs) via Multiple Imaging Modalities and Modifications to Reduce Cytotoxicity: An Educational Review," *Journal of Nanotheranostics*, vol. 1, no. 1, pp. 105–135, 2020, doi: 10.3390/jnt1010008.

[72] S. F. Shi, J. Jia, X. Guo, Y. Zhao, B. Liu, D. Chen, Y. Guo, and X. Zhang, "Toxicity of iron oxide nanoparticles against osteoblasts," *Journal of Nanoparticle Research*, vol. 14, no. 9, 2012, doi: 10.1007/s11051-012-1091-2.

[73] A. Elbakry, E. Wurster, A. Zaky, R. Liebl, E. Schindler, P. Bauer-Kreisel, T. Blunk, R. Rachel, A. Goepferich, and M. Breunig, "Layer-by-layer coated gold nanoparticles: Size-dependent delivery of DNA into cells," *Small*, vol. 8, no. 24, pp. 3847–3856, 2012, doi: 10.1002/smll.201201112.

[74] Y. Pan, S. Neuss, A. Leifert, M. Fischler, F. Wen, U. Simon, G. Schmid, W. Brandau, and W. Jahnen-Dechent, "Size-dependent cytotoxicity of gold nanoparticles," *Small*, vol. 3, no. 11, pp. 1941–1949, 2007, doi: 10.1002/smll.200700378.

[75] R. Duffin, L. Tran, D. Brown, V. Stone, and K. Donaldson, "Proinflammogenic effects of low-toxicity and metal nanoparticles in vivo and in vitro: Highlighting the role of particle surface area and surface reactivity," *Inhal Toxicol*, vol. 19, no. 10, pp. 849–856, 2007, doi: 10.1080/08958370701479323.

[76] T. T. Sibov, L. F. Pavon, L. A. Miyaki, J. B. Mamani, L. P. Nucci, L. T. Alvarim, P. H. Silveira, L. C. Marti, and LF Gamarra, "Umbilical cord mesenchymal stem cells labeled with multimodal iron oxide nanoparticles

with fluorescent and magnetic properties: Application for in vivo cell tracking," *Int J Nanomedicine*, vol. 9, no. 1, pp. 337–350, 2014, doi: 10.2147/IJN.S53299.

[77] I. Wiegand, K. Hilpert, and R. E. W. Hancock, "Agar and broth dilution methods to determine the minimal inhibitory concentration (MIC) of antimicrobial substances," *Nat Protoc*, vol. 3, no. 2, pp. 163–175, 2008, doi: 10.1038/nprot.2007.521.

[78] P. Nehra, R. P. Chauhan, N. Garg, and K. Verma, "Antibacterial and antifungal activity of chitosan coated iron oxide nanoparticles," *Br J Biomed Sci*, vol. 75, no. 1, pp. 13–18, 2018, doi: 10.1080/09674845.2017.1347362.

[79] P. V. Baptista, M. P. Mccusker, A. Carvalho, and D. A. Ferreira, "Nano-Strategies to Fight Multidrug Resistant Bacteria "A Battle of the Titans" vol. 9, no. July, pp. 1–26, 2018, doi: 10.3389/fmicb.2018.01441.

[80] M. Arakha, S. Pal, D. Samantarrai, T. K. Panigrahi, B. C. Mallick, K. Pramanik, B. Mallick, and S. Jha, "Antimicrobial activity of iron oxide nanoparticle upon modulation of nanoparticle-bacteria interface," *Sci Rep*, vol. 5, pp. 1–12, 2015, doi: 10.1038/srep14813.

[81] "Magnetic Field Effect on Growth and Antibiotic Susceptibility of Staphylococcus aureus," *Journal of Al-Nahrain University Science*, vol. 17, no. 3, pp. 138–143, 2017, doi: 10.22401/jnus.17.3.19.

[82] A. Yadollahpour, M. Jalilifar, and S. Rashidi, "Antimicrobial effects of electromagnetic fields: A review of current techniques and mechanisms of action," *J Pure Appl Microbiol*, vol. 8, no. 5, pp. 4031–4043, 2014.

[83] Q. Wang, J. Vachon, B. Prasad, C. A. Pybus, N. Lapin, R. Chopra, and D. E. Greenberg, "Alternating magnetic fields and antibiotics eradicate biofilm on metal in a synergistic fashion," *NPJ Biofilms Microbiomes*, vol. 7, no. 1, pp. 1–10, 2021, doi: 10.1038/s41522-021-00239-y.

[84] C. Xu, O. U. Akakuru, J. Zheng, and A. Wu, “Applications of iron oxide-based magnetic nanoparticles in the diagnosis and treatment of bacterial infections,” *Front Bioeng Biotechnol*, vol. 7, no. JUN, pp. 1–15, 2019, doi: 10.3389/fbioe.2019.00141.

[85] M. Taupitz, J. Schnorr, C. Abramjuk, S. Wagner, H. Pilgrimm, H. Hünigen, and B. Hamm, “New Generation of Monomer-Stabilized Very Small Superparamagnetic Iron Oxide Particles (VSOP) as Contrast Medium for MR Angiography: Preclinical Results in Rats and Rabbits,” 2000.

[86] J. Kang, C. Wang, Z. Xue, M. Liu, and H. Tan, “Buckling delamination induced microchannel: Flow regulation in microfluidic devices,” *Appl Phys Lett*, vol. 109, no. 10, Sep. 2016, doi: 10.1063/1.4962429.

[87] J. Ma, S. M. Y. Lee, C. Yi, and C. W. Li, “Controllable synthesis of functional nanoparticles by microfluidic platforms for biomedical applications-a review,” *Lab on a Chip*, vol. 17, no. 2. Royal Society of Chemistry, pp. 209–226, Jan. 21, 2017. doi: 10.1039/C6LC01049K.

[88] S. I. Hamdallah, R. Zoqlam, P. Erfle, M. Blyth, A. M. Alkilany, A. Dietzel, and S. Qi, “Microfluidics for pharmaceutical nanoparticle fabrication: The truth and the myth,” *Int J Pharm*, vol. 584, Jun. 2020, doi: 10.1016/j.ijpharm.2020.119408.

[89] Y. Song, J. Hormes, and C. S. S. R. Kumar, “Microfluidic synthesis of nanomaterials,” *Small*, vol. 4, no. 6. pp. 698–711, Jun. 2008. doi: 10.1002/smll.200701029.

[90] F. Bally, C. A. Serra, V. Hessel, and G. Hadziioannou, “Micromixer-assisted polymerization processes,” *Chemical Engineering Science*, vol. 66, no. 7. pp. 1449–1462, Apr. 01, 2011. doi: 10.1016/j.ces.2010.07.026.

[91] P. Sahariah, V. S. Gaware, R. Lieder, S. Jónsdóttir, M. Á. Hjálmarsdóttir, O. E. Sigurjonsson, M. Másson, “The effect of substituent, degree of acetylation and positioning of the cationic charge on the antibacterial

activity of quaternary chitosan derivatives," *Mar Drugs*, vol. 12, no. 8, pp. 4635–4658, 2014, doi: 10.3390/md12084635.

APPENDICES

A. Fabrication of PDMS Device and SU-8 Mold

To produce PDMS device before nanoparticle synthesis, SU-8 mold should be fabricated, which is known as master mold. SU-8 mold has prepared in cleanroom at UNAM, detailed procedure was explained below.

A.1 Silicon Wafer Cleaning

To remove all inorganic and organic dust form the 4 – inch silicon wafer, it is rinsed with acetone, isopropanol, and distilled water. The treated silicon wafer is dried with a nitrogen gun and put in an oven at 120 ° C to evaporate the moisture on the wafer.

Two layers are used to prepare the SU-8 mold. They are called base layer, which acts as a primer layer and main layer which holds the pattern. SU – 8 2005, which is used for the base layer, is an adhesive component, and prevents delamination of SU-8 mold. Thus, the mold can be reused while preparing the PDMS device.

A.2 Preparing of Base Layer

After cleaning the wafer out of oven, it is cooled to room temperature. After cooling, spinner is covered with aluminum foil and wafer is placed in chuck and vacuumed. The spin parameters are entered into the spinner, then 4 ml of SU-8 2005 is poured on the wafer, and spinning has started.

Spin parameters for the base layer are stated in Table A.1.

Table A.1 Spin Parameters for Base Layer

Step	Velocity (rpm)	Acceleration (rpm/s)	Time (s)
1	500	100	25
2	2500	200	40

After spinning is completed, wafer is placed on the aluminum foil and pre-baked process has started.

Table A.2 Pre-baked Parameters for Base Layer

Step	Temperature (°C)	Time (min)
1	65	2
2	95	4
3	65	1

After pre – baked process, to crosslink the photoresist, wafer is exposed to blank mask. The details of the process are

- Manual top side
- Contact mode = soft contact
- Separation = 100 μm
- Mask thickness = 2.3 mm
- Sample thickness = 0.5 mm
- Resist thickness = 2 μm
- Exposure intensity = 120 mJ/cm^2

After pre-baked step, post baked step is done in order to solidify the photoresist.

Table A.3 Post Baked Parameters for Base Layer

Step	Temperature (°C)	Time (min)
1	65	1
2	95	3
3	65	1

A.3 Main Layer Preparation for Microchannel Mold

After base layer completed, main layer will be processed to obtain microchannel mold. For main layer, the spin parameters are set as follows,

Table A.4 Spin Parameters for Second Layer

Step	Velocity (rpm)	Acceleration (rpm/s)	Time (s)
1	500	50	40
2	2200	300	35

Before starting the spin process, the spinner is covered with aluminum foil, a silicon wafer is mounted in chuck, and applied vacuum. 4 ml of SU-8 2005 is poured into the center of the wafer, and the spinning process is then initialized.

After spinning is executed, SU-8 was removed smoothly by using glass slide from the edges of the circular wafer. It is placed on the aluminum foil to start pre – baked step for second layer.

Table A.5 Pre – baked for second layer

Step	Temperature (°C)	Time (min)
1	65	3
2	95	8
3	65	2

Exposure should be done after the wafer to cool to room temperature again as mentioned before in the spin coating section. Details of the process are,

- Manual top side
- Contact mode = soft contact
- Separation = 200 μm
- Mask thickness = 2.3 mm

- Sample thickness = 0.5 mm
- Resist thickness = 100 μm
- Exposure intensity = 230 mJ/cm^2

After exposure step, post – baked process is done.

Table A.6 Post – baked parameters for main layer

Step	Temperature (°C)	Time (min)
1	65	3
2	95	8
3	65	2

After solidification of the photoresist, the wafer is cooled to room temperature. SU – 8 developer is added to the beaker, wafer is immersed in it and mixed for 9 min. If agitation is rapid, wafer might be damaged or if agitation is low, uniform distribution of developer on the wafer is not provided. After 9 min, wafer is rinsed with water and isopropanol and then dried with nitrogen.

B. Preparing PDMS Microreactor Using SU – 8 Mold

Using produced SU – 8 mold, PDMS device were fabricated. First of all, PDMS base and curing agent (10:1) were mixed for 3 min and pour onto silicon wafer for preparation. Then, the silicon wafer with the mixture was put in a vacuum pump to remove air bubbles for 20 min. After degassing, silicon wafer with mixture was put into oven to crosslinking of PDMS mixture at 80 °C for 30 min. Then, the cured PDMS layer was peeled off from the silicon wafer, the holes for the the tubing were opened for inlet and the outlet, and PDMS layer was bonded to the glass slide to close microchannels.